January 2015

Microscale Radiometer Based on the Knudsen Thermal Force

Andrew Strongrich
Purdue University

PURDUE UNIVERSITY
GRADUATE SCHOOL
Thesis/Dissertation Acceptance

This is to certify that the thesis/dissertation prepared

By Andrew David Strongrich

Entitled
MICROSCALE RADIOMETER BASED ON THE KNUDSEN THERMAL FORCE

For the degree of Master of Science in Aeronautics and Astronautics

Is approved by the final examining committee:

Alina Alexeenko
Chair

Martin Corless

Steven Wereley

Amy Marconnet

To the best of my knowledge and as understood by the student in the Thesis/Dissertation Agreement, Publication Delay, and Certification Disclaimer (Graduate School Form 32), this thesis/dissertation adheres to the provisions of Purdue University's "Policy of Integrity in Research" and the use of copyright material.

Approved by Major Professor(s): Alina Alexeenko

Approved by: Tom Shih 11/13/2015
Head of the Departmental Graduate Program Date

MICROSCALE RADIOMETER BASED ON THE KNUDSEN THERMAL FORCE

A Thesis

Submitted to the Faculty

of

Purdue University

by

Andrew D. Strongrich

In Partial Fulfillment of the

Requirements for the Degree

of

Master of Science

December 2015

Purdue University

West Lafayette, Indiana

Dedicated to my parents for their unwavering support in all that I do.

ACKNOWLEDGMENTS

I would like to thank my advisor, Professor Alina Alexeenko, for her confidence and trust in my abilities. I am eternally grateful for the opportunity she has afforded me and could not have pursued my graduate studies without her support. I would like to thank Professor Dimitri Peroulis for his patience in early stages of research and the advice he offered related to microsystem design.

I would like to thank Tony Cofer for his kindness, mentorship, and guidance through the years. I continually aspire to achieve his level of ingenuity and resourcefulness. I would also like to thank Michael Sinani, Nithin Raghunathan, and the rest of the Birck Nanotechnology Center staff for cleanroom training and fabrication advice.

I would like to thank Ted Sieffert for his unparalleled friendship, loyalty, and dependability throughout my undergraduate and graduate careers. Sam Zanker and her family for their incredible support and hospitality. Dave Schulz for our time cycling together and the times that were had. David Kun for pushing me to go the extra mile. Finally, and most of all, my parents for making all of this possible.

TABLE OF CONTENTS

Page

LIST OF TABLES

LIST OF FIGURES

SYMBOLS

Kn	Knudsen number
λ	Molecular mean-free path
L	Length
μ	Dynamic viscosity
p	Pressure
k_B	Boltzmann's constant
T	Temperature
m	Molecular mass
A	Wetted area between heater and shuttle arms
k	Suspension spring constant
E	Young's modulus
$I_{z,b}$	Moment of inertia in the out-of-plane direction
N	number of elements
w	Width
R	Resistance
V	Voltage
P	Power
F	Force
C	Capacitance
ϵ_0	Vacuum permittivity
ϵ_r	Relative permittivity
d	Device layer thickness
e	Capacitor comb finger separation
g	Gap separating heater and shuttle arms
t	Time

ω	Charge integrator input voltage frequency
θ	Phase angle
Λ	Lock-in amplifier output voltage calibration factor
p	Curve fit coefficient for spring constant calibration

Subscripts

mdr	Meander
flx	Flexure
$shnt$	Shunt
$shtl$	Shuttle
$heat$	Heater arm
sen	Sense
act	Actuation
fbk	Feedback
ref	LIA reference
∞	Ambient conditions
I	Charge integrator output
LIA	LIA output
ES	Electrostatic
$damp$	Gas damping
Kn	Knudsen force

ABBREVIATIONS

LIA	Lock-in amplifier
MEMS	Microelectromechanical system
CAD	Computer-aided drafting
PSD	Phase-sensitive detector
ES-BGK	Ellipsoidal statistical Bhatnagar-Gross-Krook
DC	Direct current
LPCVD	Low pressure chemical vapor deposition
PR	Photoresist
HMDS	Hexamethyldisilizane
HF	Hydrofluoric acid
DI	Deionized
IPA	Isopropanol
LCC	Leadless chip carrier
PCB	Printed circuit board
SEM	Scanning electron microscope
DAQ	Data acquisition
PI	Proportional-integral

ABSTRACT

Strongrich, Andrew D. MS, Purdue University, December 2015. Microscale Radiometer Based on the Knudsen Thermal Force. Major Professor: Alina A. Alexeenko.

Radiometric phenomena arise in non-isothermal rarefied gas flows for which the molecular mean-free path is approximately equal to the characteristic scale of the temperature gradient. The non-equilibrium nature of these flows results in thermal stresses which are capable of exerting forces and moments on immersed structures. When the stresses are established between unequally heated bodies the forces are referred to as Knudsen thermal forces. This work presents the design, fabrication, and characterization of a novel in-plane microscale radiometer capable of both producing and resolving Knudsen forces in low pressures. The current work differs from previous implementations in that both capacitance and temperature measurements are acquired simultaneously, extending permissible measurement range by up to 3 pressure decades. Sensitivity to ambient pressure, temperature gradient, as well as gas composition is demonstrated, illustrating the mechanism's versatility in measuring various macroscopic fluid properties. For constant input power force output is shown to vary non-monotonically with ambient pressure, having peak magnitude at a Knudsen number of approximately unity. Using thermal microscopy, results are presented in terms of a non-dimensional force coefficient, showing output enhancement of over 7 times at peak magnitude compared to existing out-of-plane cantilevered configurations.

1. INTRODUCTION

Temperature inhomogeneities in rarefied gases give rise to thermal stresses which, in turn, are capable of inducing bulk fluid flows and exerting forces on immersed structures [18]. Manifestations of these stresses are frequently misnomered "radiometric" phenomena after it was originally believed the effects were a result of the momentum of radiation [9, 24, 4]. The physical nature of thermally induced flows has been studied for centuries however a collective effort to describe the underlying physics was largely kindled by Sir William Crookes in the 1870's after the development of his famous radiometer [4, 5]. Crookes' device consists of a series of vanes similar to that shown in Figure 1.1 which revolve around a central spindle in a partially evacuated bulb.

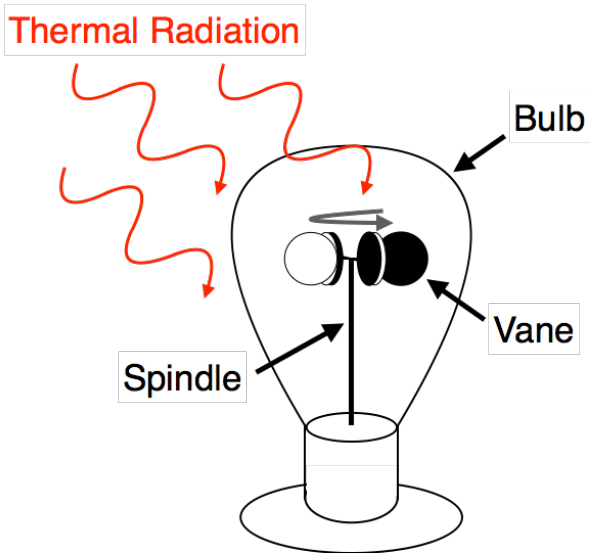

Figure 1.1. Crookes' radiometer

One side of the radiometer vanes is painted such that it has a higher emissivity than the opposing face, allowing it to better absorb radiation. When illuminated by a light

source of sufficient intensity the thin vanes develop a strong thermal gradient through their thickness and begin to revolve around the spindle in opposite direction (i.e. hot to cold). Crookes and others attributed the effect to photon pressure however after a series of experiments by Schuster [30] and theoretical treatment by Reynolds [28] it was suggested that force generation instead manifests within surrounding low-pressure gas. It was later shown in various works that the exact mechanisms governing force production are dependent on the thermal gradient magnitude and direction, device configuration, ambient pressure, as well as fluid composition [16].

Radiometric forces achieve their maximum in the transitional rarefied flow regime when the fluid admits neither a free-molecule nor continuum treatment [32]. Generally, these two limits are defined by the non-dimensional Knudsen number, the ratio of the molecular mean-free path to the characteristic length scale of the macroscopic gradients or geometry [1]. In terms of the dynamic viscosity,

$$Kn = \frac{\lambda}{L} = \frac{\mu}{p_\infty L}\sqrt{\frac{2k_B T_\infty}{m}} \tag{1.1}$$

The total force acting on a radiometer vane stems from a combination of the so-called area, edge, and shear effects, each of which is illustrated in Figure 1.2.

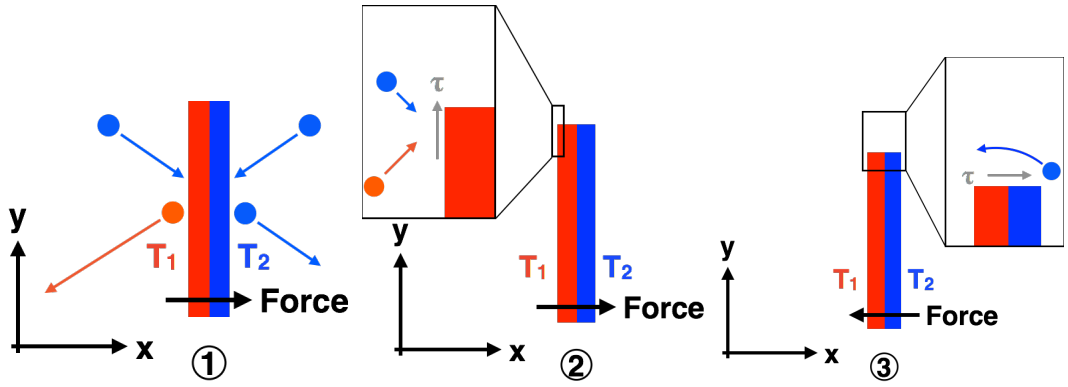

(a) Area effect (b) Edge effect (c) Shear effect

Figure 1.2. Forces mechanisms in Crookes' radiometer

For large Knudsen numbers ($Kn \gg 1$), force generation manifests through direct kinetic energy exchange between molecules and the vane. This concept is referred to as the area effect [33] and is illustrated in Figure 1.2(a). Assuming uniform temperature far-field boundary conditions, all molecules incident to the vane surface have equal kinetic energy and thus impart equal momentum upon collision, ultimately resulting in zero net force. For a fully diffuse gas-surface interaction, molecules interacting with the heated side accumulate more kinetic energy after the collision than those at the cooler side and are thus reflected with greater momentum. This imbalance among emitted species leads to the production of a force along x-coordinate in a direction opposite the thermal gradient (hot to cold), acting uniformly over the entire surface.

For small Knudsen numbers ($Kn \ll 1$) the flow enters the continuum limit and the radiometric force becomes dominated by thermal stresses within the gas. This behavior can be qualitatively discussed through expansion of the velocity distribution function in the Knudsen number via the Chapman-Enskog method [3]. This technique yields the Euler equations if carried out to the zeroth order followed by the Navier-Stokes equations if expanded to the first order. The second order expansion yields the more complicated Burnett equations. Comparison of the Burnett stress terms to those of Navier-Stokes leads to additional forces scaling with Kn^2 which are dependent on thermal gradients within the fluid [10]. For sufficiently low speed highly non-isothermal flows it has been shown that these terms can become significant, leading to the generation of a temperature induced convection [18].

For low Knudsen number flows the area effect no longer contributes substantially to force generation and instead most of the momentum transfer occurs near the free edge [32, 33]. This is referred to as the edge effect and is represented in Figure 1.2(b). Here, the isothermal contours are sharply curved and thermal gradients in the y-direction can become large. Considering an area of a few mean-free paths from the edge of the vane the small surface will be struck by both high temperature molecules inside the perimeter as well as cooler molecules from outside. Assuming a uniform pressure distribution throughout the vessel the temperature ratio (T_2/T_1) for incident

species leads to a number density ratio of $n_2/n_1 > 1$. In terms of molecular number flux, this leads to $\dot{N}_2/\dot{N}_1 \approx \sqrt{T_1/T_2} > 1$. Similar to the area effect, the high number density species striking the vane surface near the edge leads to a local increase in momentum flux upon emission. The discrepancy in molecular velocity near the edge also leads to the development of a shear stress on the vane in the y-direction which, in turn, induces fluid motion towards the centerline. This behavior is referred to as thermal edge flow and contributes to the formation of large vortical structures which have been shown to surround the vane [36, 40].

Finally, the temperature gradient through the thickness of the vane induces thermal creep stress in the gas which leads to fluid motion from the cold side to the hot side. This forms the shear effect [12], the result of which is portrayed in Figure 1.2(c). Following an analytical treatment by Scandurra et al. it is expected that the motion of the gas across vane surfaces will form a shear stress on the thin edge which complements the forces generated by both the area and edge effects [29]. In a numerical study using both the deterministic ES-BGK and stochastic DSMC methods however it was found that the shear contribution actually opposes the forces induced by the area and edge forces. Nevertheless, the contribution from shear is minimal, contributing less than 10% to total force production [31].

1.1 The Knudsen Thermal Force

When two solid boundaries of unequal temperature are used to establish the thermal gradient within a rarefied system, the thermal stresses are known as Knudsen forces. The principles governing the behavior of these stresses are fundamentally similar to those surrounding the radiometer vane. For uniformly heated bodies the Knudsen force is repulsive in nature, exhibiting peak magnitude between the free-molecule and continuum limits when the mean-free path of the gas is approximately equal to the gap separating the surfaces [25, 26]. Exploitation of this effect was first realized by Knudsen in 1910 whereby using kinetic theory he developed an expression

for force magnitude based solely on the ambient pressure of the gas and temperature of the boundaries. For this reason, such devices are commonly referred to as Knudsen gauges. Knudsen gauges have traditionally been implemented to measure ambient gas pressure in high-vacuum, however it has been shown they also have utility elsewhere such as in measuring the vapor pressure of metals [14]. Two typical configurations are represented in Figure 1.3.

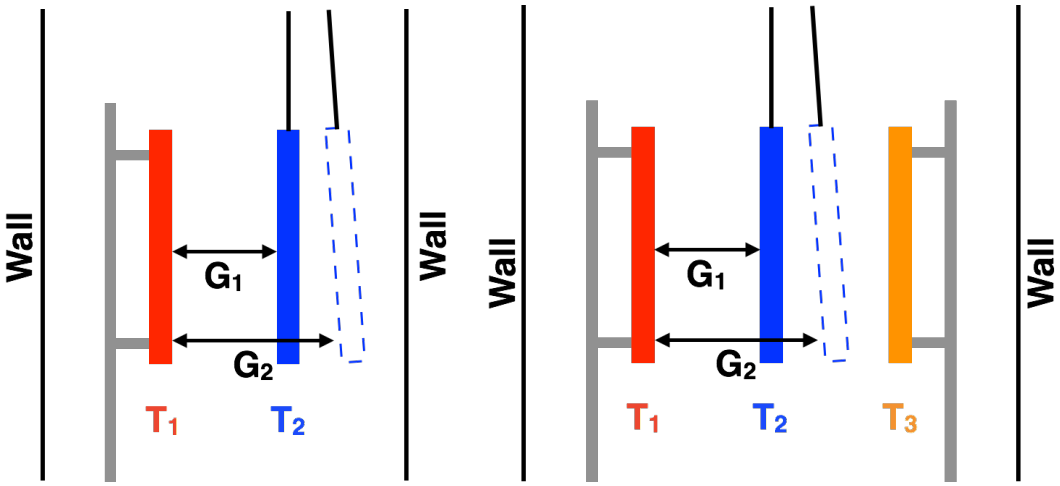

(a) 2-plate Knudsen gauge (b) 3-plate Knudsen gauge

Figure 1.3. Typical Knudsen gauge configurations

Considering the gauge from Figure 1.3(a), the device consists of two plates maintained inside of a vacuum chamber. Plate 1 is fixed, containing a series of heating elements to raise its temperature above that of the surroundings. Plate 2 is unheated and suspended by a thin filament, permitting it to freely displace in response to Knudsen forces. Through calibration against a reference gauge the chamber pressure can be evaluated directly through measurement of the plate separation provided their respective temperatures remain constant. Following the original derivation by Knudsen [17], it can be shown that for devices operating in a regime for which the Knudsen number is large the force dependence is linear with pressure. The force acting between the bodies in Figure 1.3(b) can be expressed by

$$F = \frac{p_\infty A}{2}\left(\sqrt{\frac{T_1}{T_2}} - 1\right) \tag{1.2}$$

In the framework of Knudsen, equation 1.2 was later modified to account for the effects of incomplete gas-surface accommodation [41, 36] as well as arbitrary 3-dimensional geometries [37]. More recently, it has been shown that application of a thermal gradient within the of the suspended body (similar to a Crookes radiometer vane) using a thermoelectric heating element can lead to either force enhancement or direction reversal depending on the gradient orientation (bias polarity), increasing the measurement sensitivity and enabling bi-directional actuation [38].

Expanding on the 2-plate Knudsen gauge of Figure 1.3(a), Lockenvitz [23] and Wu [42] introduced a third fixed plate on the exposed side of the suspended element having a temperature which is different from the two original bodies. The geometry is shown in Figure 1.3(b). Through this implementation it can be shown that force magnitude is independent of the temperature of plate 2 and is described by equation 1.3 if plate dimensions are identical. The simplification gained by the temperature independence of the suspended vane overcomes one of the principle difficulties associated with the simpler 2-plate configuration.

$$F = \frac{p_\infty A}{2}\left(\sqrt{\frac{T_1}{T_\infty}} - \sqrt{\frac{T_3}{T_\infty}}\right) \tag{1.3}$$

Regardless of configuration, the macroscopic size Knudsen gauges combined with their ability to operate linearly only in the free-molecule regime has traditionally confined these devices to the measurement of only very low pressures ($\leq 10^{-5}$ Torr). With the addition of their high sensitivity to external vibrations and lack of electronic instrumentation these devices received limited implementation outside of laboratory environments [37].

1.1.1 Microscale Knudsen Gauges

With the advent of the microelectronics industry in the 1980s came the capability of fabricating mechanical structures having microscale geometries. One of the principle disadvantages of Knudsen gauges, their macroscopic size, can be overcome through application of these micromachining techniques, shifting the usable range pressure range upwards by 5 to 6 decades. The potential of exploiting this effect using a MEMS device was first realized by Passian et al. [27] whereby a microcantilever was heated by means of a chopped laser and the corresponding out-of-plane deflection was sensed capacitively over a range of operating pressures from less than 100 Pa to 1 atmosphere [26]. This concept was extended by Sista and Bhattacharya using a suspended Joule heated proof mass [35]. Actuation of a cool hinged flap structure away from a heated substrate has also been successfully demonstrated as an alternative method of force generation [15]. Although these microscale implementations are able to shift the usable range of the Knudsen gauge to more reasonable pressures, they are not able to overcome the limitations imposed by the non-monotonically varying force magnitude, limiting their utility to only highly rarefied environments.

In this work, I detail the design and development of a novel Microelectromechanical In-plane Knudsen Radiometric Actuator (MIKRA) capable of producing and resolving Knudsen forces over a wide range of operating pressures as well as for different fluid mediums and device temperatures. The operational constraints imposed on existing microscale systems are overcome with the addition of temperature dependent resistance measurements, allowing pressure to be uniquely defined over the entire range of which Knudsen forces are appreciable. The demonstrated combined sensitivity to gas composition, pressure, and temperature gradient gives this sensing mechanism promise in applications ranging from the lyophilization of food and pharmaceuticals to high-altitude vehicles such as satellites and weather balloons.

2. MICROSCALE RADIOMETRIC ACTUATOR DESIGN

The design of the MIKRA device is centered around a floating shuttle-mass architecture which is able to actuate in the plane of an underlying substrate. Previous MEMS-scale Knudsen gauge applications derive their operation from the out-of-plane actuation of a cantilever or proof mass [26, 35]. Although this method offers the combined advantages of both fabrication and design simplicity it does not easily facilitate the direct measurement of structure displacement, making quantification of Knudsen force magnitude difficult. The MIKRA device consists of 5 primary components: the shuttle, the suspension, heating elements, sense capacitors, and actuation capacitors. A CAD representation of the device with components labeled is shown in Figure 2.1.

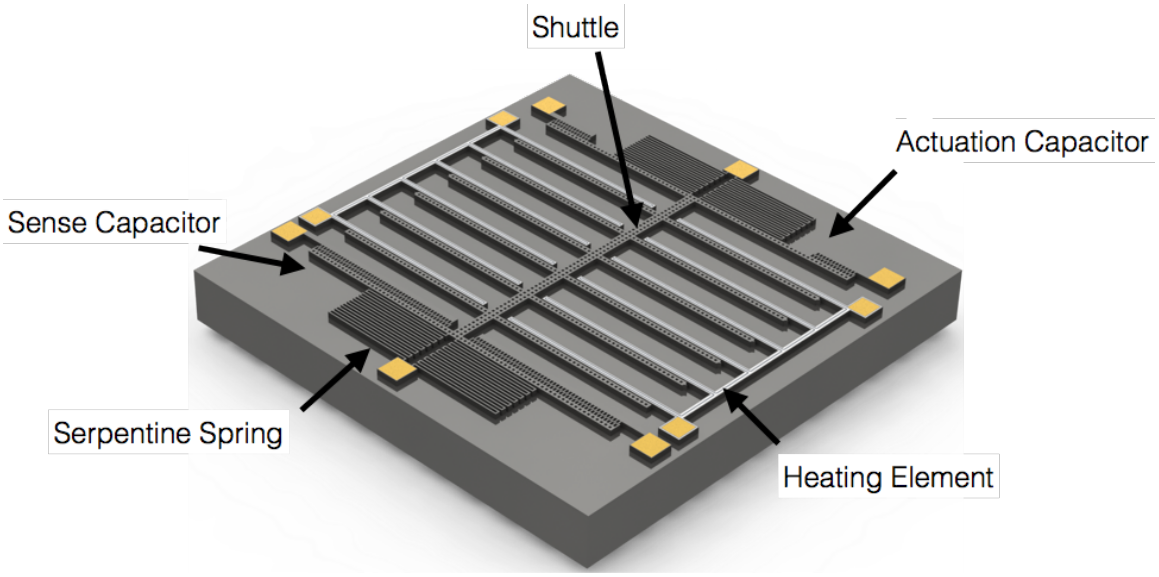

Figure 2.1. CAD representation of MIKRA device

The shuttle-mass consists of a long central support member 2.57 mm in length and 50 μm thick having a series of 12 evenly spaced reaction arms extending trans-

versely outwards a distance of 1.41 mm from its axial direction. The shuttle assembly itself is suspended 4 μm above an underlying substrate by a series of 4 serpentine springs in parallel configuration. To form the gradient needed for Knudsen force generation a series of fixed heater arms are held adjacent to the movable shuttle arms a distance of 20 μm away. As the shuttle deflects under the action of the induced forces its displacement is sensed by an array of comb capacitors. This capacitance measurement, in turn, provides a measure of force magnitude if properly calibrated. The measurement concept is illustrated in Figure 2.2, showing the interaction of a single heater and shuttle arm pair.

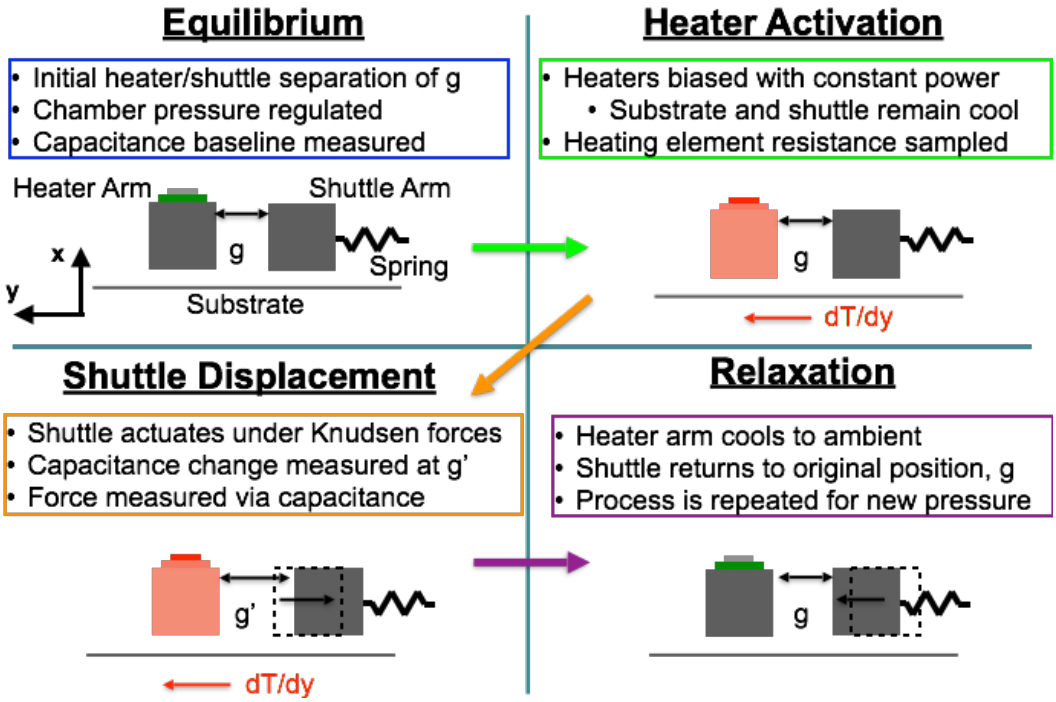

Figure 2.2. MIKRA measurement concept

The detailed design of MIKRA's principle elements is discussed in the subsequent sections.

2.1 Suspension

Owing to their radiometric nature Knudsen force magnitudes are inherently small, typically assuming values on the order of ∼100 μN/m [25]. To achieve a measurable deflection of the shuttle away from the heating elements its suspension must necessarily be highly compliant, ideally on the order of ∼1 N/m. For this reason a serpentine configuration was selected, the geometry of which is shown in Figure 2.3.

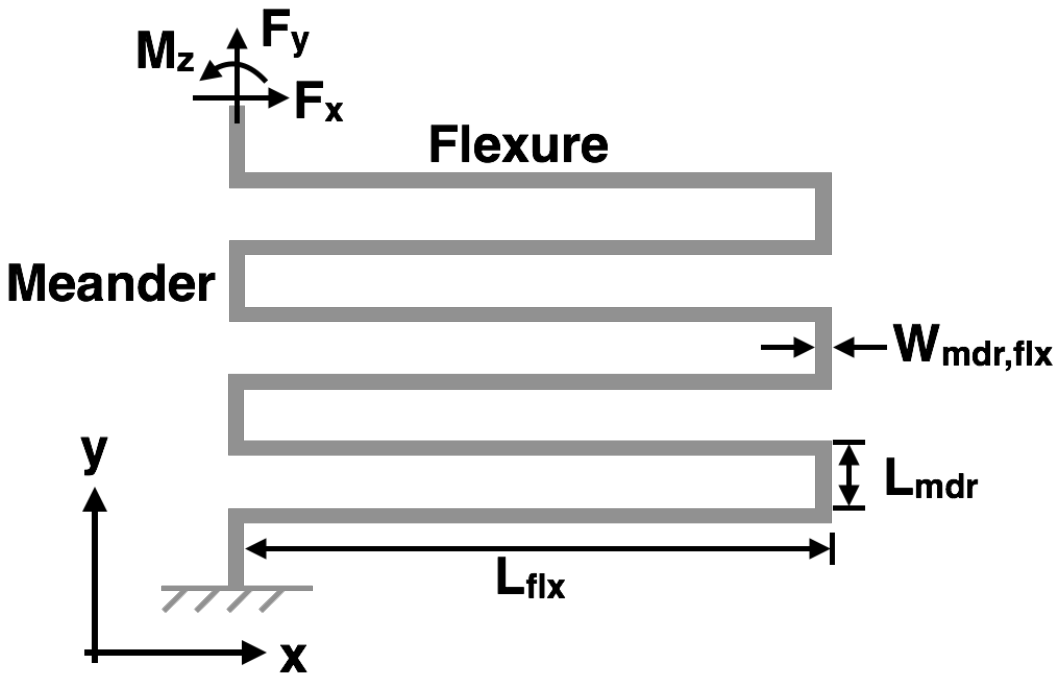

Figure 2.3. Serpentine suspension schematic

Serpentine suspensions consist of alternating series of meanders and flexures and exhibit greatest compliance in the axial (y-coordinate) direction. Forming the structure in this way has the benefit of conserving space along the same dimension. Alternative configurations such as those involving tapering or non-uniform flexure lengths can be found in the literature [22].

2.1.1 Analytical Suspension Modeling

During initial design the serpentine suspension is constrained only by its meander and flexure width, a fabrication limitation imposed by optical lithography. From basic mechanics it is known that the stiffness of the structure scales with the cube of this parameter and should thus be minimized. For these reasons the suspension width was chosen to be 10 μm. Performing the static force and moment balance and employing the principles of Castigliano the spring constant in the shuttle axial coordinate direction is provided in equation 2.1. It should be noted that this relation applies only to springs having an odd number of meanders as well as uniform width and thickness among all members. Expressions for the transverse and out-of-plane direction can be found in the reference [7].

$$k_y = \frac{12EI_{z,b}((L_{mdr} + L_{flx})N_{mdr} - L_{flx})}{L_{flx}^2(N_{mdr} - 1)((3L_{mdr}^2 + 4L_{mdr}L_{flx} + L_{flx}^2)N_{mdr} + 3L_{mdr}^2 - L_{flx}^2)} \tag{2.1}$$

From equation 2.1 it can be seen that for a given flexure and meander width the suspension compliance in the actuation direction is most effectively optimized via the flexure length and meander quantity. These parameters cannot be maximized arbitrarily however as the advantage of increased sensitivity is offset by a decreased resistance external shock, potentially leading to shuttle stiction as a result of contact with the substrate. Additional consideration must also be given to the fabrication process as high aspect ratio structures are not easily etched using standard micromachining methods.

2.1.2 Finite Element Modeling of Suspension

To verify the accuracy of the analytical model finite element simulations were carried out for a flexure length of 600 μm using ANSYS APDL. A total of 2 boundary conditions are needed to define the model: a rigid or fixed condition at the anchor and a remote displacement at the shuttle. The use of a remote displacement stems from

the condition of symmetry, permitting only a translation of the boundary surface. The geometry was simulated under various loading conditions, both in magnitude and direction. Using this sweep scheme the spring deflection is shown to vary linearly with load magnitude in all 3 coordinate dimensions, permitting the implementation of Hooke's law in the modeling of system dynamics. This behavior is shown in Figure 2.4 for a Young's modulus and Poisson's ratio of 166 GPa and 0.3 respectively.

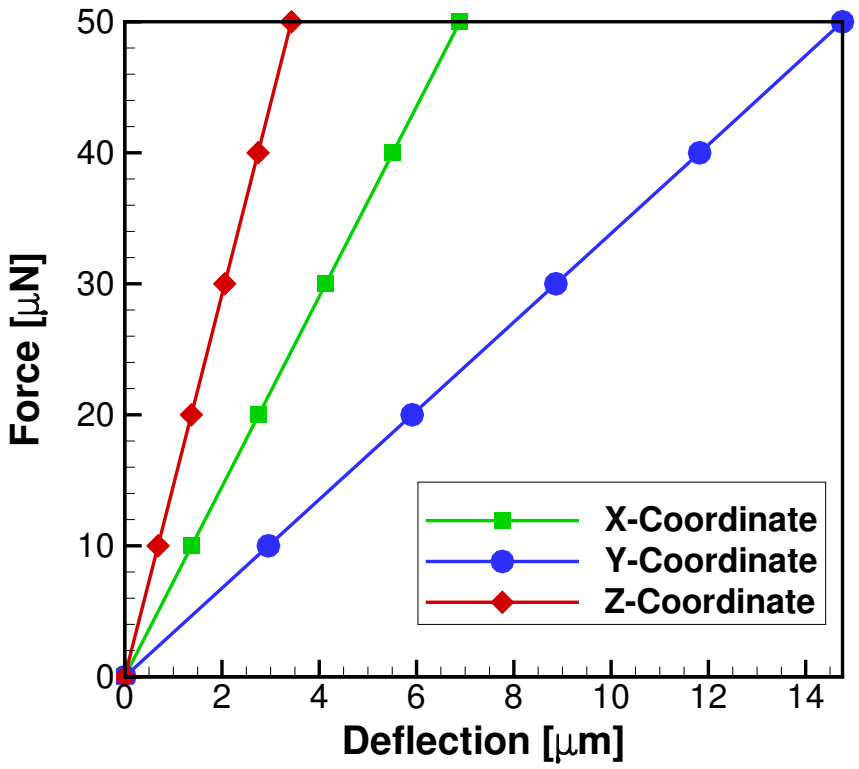

Figure 2.4. Serpentine suspension deflection behavior from finite-element simulations

As a result of the linear deflection behavior with applied load linear least-squares fit from Figure 2.4 can be used to evaluate the spring constant of the suspension system. A comparison of results from the finite element simulations to the analytical model for a single spring element is provided in Table 2.1.

Table 2.1. Comparison of spring constants for 600 μm flexure length with 15 meanders

	Analytical [N/m]	**Numerical [N/m]**	**Percent Difference**
k_x	5.302	7.256	26.9%
k_y	2.365	3.387	30.2%
k_z	47.308	14.586	224.3%

From Table 2.1 it can be seen that the analytical and numerical results agree only modestly for constants k_x and k_y and rather poorly for k_z. These errors likely stem from the short meander lengths relative to beam width, allowing nonlinear expansion and contraction effects to become significant. This behavior cannot be effectively captured by the analytical approach. Nevertheless, the analytical model can be employed as a method of preliminary suspension design.

The suspension geometry should be selected so as to provide sufficient compliance in the axial shuttle direction to permit appreciable motion under the action of Knudsen forces while also maintaining suitable stiffness in the transverse and vertical directions for shock resistance. With these considerations the parameters of the selected suspension element are provided in Table 2.2.

Table 2.2. Selected dimensions of serpentine suspension

Parameter	**Value**	**Unit**
$w_{mdr,flx}$	10	μm
L_{mdr}	30	μm
L_{flx}	600	μm
N_{mdr}	15	μm

2.2 Heating Elements

Deposited over the upper surface the heating arms are continuous heating elements 10 μm wide and 100 nm thick which are designed to be resistively heated at an arbitrarily specified power. The heating element material is chosen to be platinum due to its known linear variation in resistance with temperature [21]. This attribute permits the monitoring of average heater temperature and hence allows the MIKRA sensor to also function similar to a pirani gauge. The small Biot number associated with the silicon structure ensures the heating arms will be uniformly heated through their thickness. As a result of the high resistance associated with thin films the heating elements must be driven with high voltages and low currents. Although this necessitates the use of a high voltage power supply it prevents the electromigration of filament material by maintaining low current density [2]. To permit automated control of heater power using a data acquisition system (low output voltages and currents) the heaters are driven by a cascaded high voltage NPN/PNP current amplifier. A schematic of this circuit is provided in Figure 2.5.

The high voltage power distribution rail is connected directly to the emitter of the KSP92TA PNP transistor. The base of the PNP is fed through a current limiting resistor into the collector of the MPSA42 NPN transistor. The base of the NPN is driven by a low power data acquisition device, the output of which leads to an amplified current through the heating element. In this case, the amplification factor is the product of both the NPN and PNP transistor gains. Designing the current amplifier in this way not only allows very small input currents to drive large loads but also allows the heating element to remain grounded when no current is supplied by the data acquisition system.

To actively regulate power dissipated by the heating element both the filament current as well as the voltage across its terminals need to be simultaneously monitored. Current is evaluated using Ohm's law by measuring the voltage drop across a shunt resistor of known value which is in series with the heating element. The

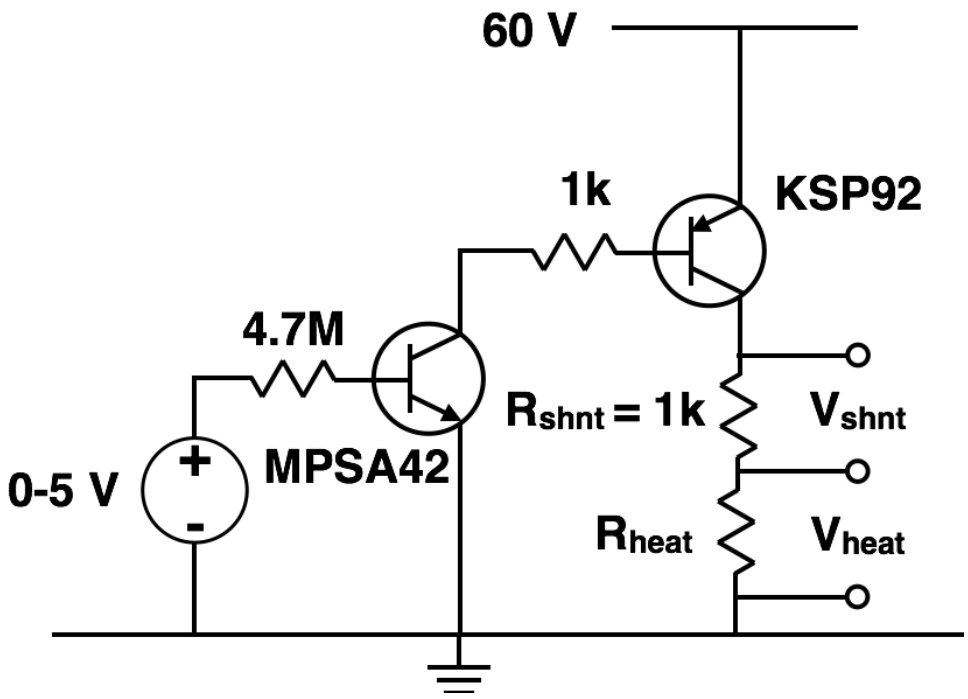

Figure 2.5. Current amplifier circuit used to drive heating elements

measured shunt resistance values are 1009.0 and 1000.4 Ω for heating elements 1 and 2 respectively. Resistances of this magnitude were selected so as to provide a measurable potential drop across their ends. Voltage across the heating element is measured using a 4-wire technique, minimizing the influence of lead resistance on measurement error. Thus the power dissipated by the heating element can be described simply by

$$P_{heat} = \frac{V_{heat} V_{shnt}}{R_{shnt}} \tag{2.2}$$

Using equation 2.2 dissipated power can be regulated via a suitably tuned PI controller, the output of which directly drives the base of the NPN transistor from Figure 2.5. Using the same parameters the total heater resistance can also be computed via

$$R_{heat} = \frac{V_{heat} R_{shnt}}{V_{shnt}} \tag{2.3}$$

The measurement of heating element resistance provides a direct measure of average filament temperature if properly calibrated against a thermal microscope. This capability gives MIKRA additional sensing benefits as will be seen when discussing experimental results.

2.3 Capacitors

The MIKRA device houses two sets of capacitors: one for the purpose of shuttle position sensing and the other for electrostatic actuation. The two primary architectures used in MEMS technology are the parallel plate and comb configurations. Both geometries are shown in Figure 2.6.

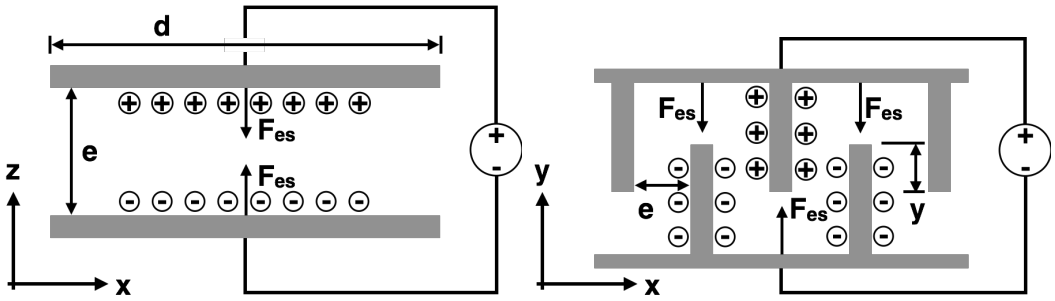

(a) Parallel-plate capacitor (b) Comb capacitor

Figure 2.6. Typical micromachined capacitor configurations

The capacitance of a circuit element is essentially of measure of its energy storage capacity. Provided the overlap area of the capacitor elements is large relative to their separation the capacitance takes on the expression

$$C = \frac{\epsilon_0 \epsilon_r d}{e} y \tag{2.4}$$

Neglecting the influence of fringe fields the expression for capacitance in equation 2.4 can be employed for either geometry in Figure 2.6. Taking the partial derivative of equation 2.4 with respect to the direction of actuation it can be seen that the capacitance variation for the comb geometry is independent of shuttle position

whereas that for the parallel plate configuration varies with $1/e^2$. As a result of its inherent simplicity and constant sensitivity regardless of engagement distance the comb capacitor configuration from Figure 2.6(b) was selected for the purpose of shuttle position sensing [34].

The act of biasing the capacitive elements for the purpose of either position detection or actuation inevitably induces electrostatic forces. This force is determined through differentiation of the stored potential energy of the capacitor in the direction of motion. Using the known capacitance from 2.4 the force for the comb configuration is described by

$$F_{es} = \frac{\partial}{\partial y}\left(\frac{1}{2}CV^2\right) = \frac{\epsilon_0 \epsilon_r d}{2e}V^2 \tag{2.5}$$

Here, it can be seen that another advantage of the comb drive lies in its independence of force output with finger engagement. For parallel plate capacitors this independence is not observed and there exists a pull-in voltage for which the device becomes unstable. With the comb drive the shuttle can, in principle, be displaced to any arbitrary position and the resulting shuttle deflection due to Knudsen forces will depend only on the spring constant. For this reason both sense and actuation capacitors have been included into the design of the MIKRA sensor.

2.3.1 Sense Capacitors

The sense capacitors are used to measure shuttle deflection in response to the Knudsen forces. These capacitors have a nominal initial overlap distance of 15 μm and can be extended to a maximum of 35 μm at gap closure. There are a total of 184 comb finger pairs with each finger having a nominal separation of 5 μm.

To measure the capacitance of the sense combs, and hence the position of the shuttle, a charge integrator circuit is employed. A schematic representation of the signal conditioning circuitry is shown in Figure 2.7.

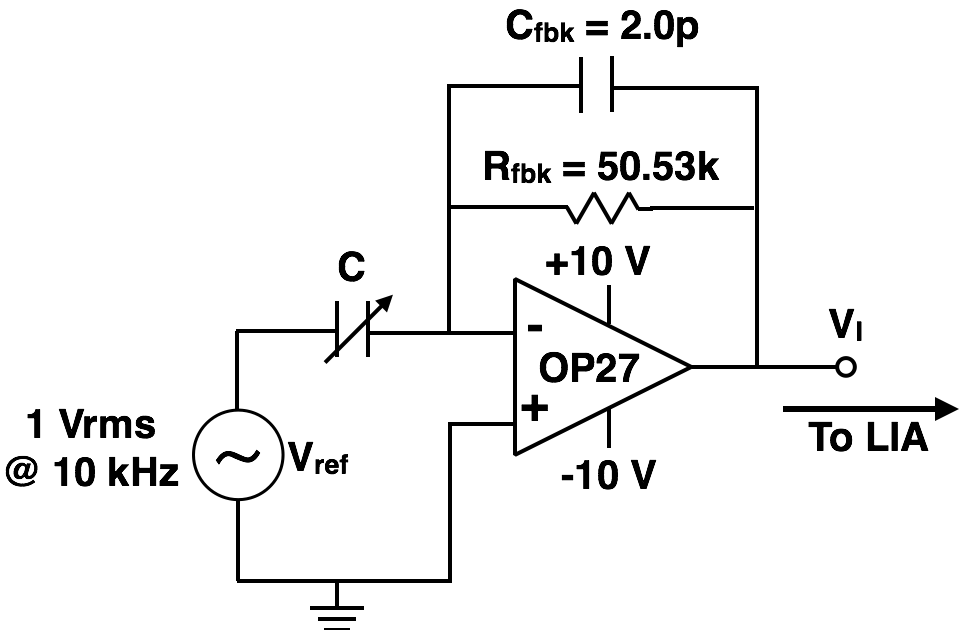

Figure 2.7. Charge integrator circuit used for shuttle displacement sensing

The circuit relies on the use of an operational amplifier to perform the integration. The non-inverting terminal of the op-amp is connected directly to earth ground, providing a corresponding virtual ground at the inverting input. The test capacitor, C, is connected to the inverting input and is driven by a known sinusoidal waveform. The op-amp output is fed back to the inverting input using a 2 pF capacitor and 50.53 kΩ resistor in parallel. Using Kirchoff's current conservation law the circuit output voltage can be modeled by

$$\frac{dV_I}{dt} + \frac{1}{R_{fbk}C_{fbk}}V_I = -\frac{C}{C_{fbk}}V_{ref}\omega_{ref}\cos\omega_{ref}t \tag{2.6}$$

Solving the non-homogenous differential equation, the output voltage becomes

$$V_I(t) = -V_{ref}CR_{fbk}\omega_{ref}\frac{C_{fbk}R_{fbk}\omega_{ref}\sin(\omega_{ref}t) + cos(\omega_{ref}t)}{(C_{fbk}R_{fbk}\omega_{ref})^2 + 1} \tag{2.7}$$

Using equation 2.7 it can be seen that the amplitude of the op-amp output varies linearly with sense capacitance. Further, an increase in shuttle/heater separation under the action of Knudsen forces leads to a decrease in capacitance and ultimately

a decrease in output amplitude. Assuming Knudsen force magnitude is on the order of 100 μN/m the theoretical spring constant suggests the shuttle will displace a distance on the order of a few hundred nanometers, corresponding to a change in capacitance on the order of femtoFarads and integrator output voltage on the order of 10 μV. To measure these small amplitude changes a lock-in amplifier is employed.

Lock-in Amplifier Operation

LIAs are typically used in environments where the noise-to-signal ratio is extremely high. To perform this task the LIA drives a system, in this case the op-amp integration circuit from Figure 2.7, with a periodic signal at a precisely known amplitude, frequency, and phase. The output of the system is in turn fed back to the amplifier filtered and amplified. The reference and output waveform are then multiplied together leading to the output

$$V_{LIA} = V_{ref} V_I sin(\omega_{ref} t + \theta_I) sin(\omega_I t + \theta_{ref}) \tag{2.8}$$

Assuming the integrator output is at the same frequency as the driving waveform equation 2.8 with some manipulation reduces to

$$V_{LIA} = \frac{1}{2} V_{ref} V_I cos(\theta_I - \theta_{ref}) + \frac{1}{2} V_{ref} V_I cos((\omega_{ref} + \omega_I)t + \theta_{ref} + \theta_I) \tag{2.9}$$

The resulting waveform contains a DC component with scaling factor based on the phase shift across the integrator as well as a sinusoid at twice the driving frequency. This high frequency component is easily removed using a high order low-pass filter, leading to the output

$$V_{LIA} \approx \frac{1}{2} V_{ref} V_I cos(\theta_I - \theta_{ref}) \tag{2.10}$$

Here the LIA output is a pure DC signal scaled by the phase shift. For this reason LIAs are also referred to as phase-sensitive detectors. By simultaneously passing the

original measured waveform through a second PSD with the reference oscillator phase shifted by 90° the resulting DC component becomes

$$V_{LIA} \approx \frac{1}{2} V_{ref} V_I sin(\theta_I - \theta_{ref}) \tag{2.11}$$

Finally, combining equations 2.10 and 2.11 the phase dependence can be eliminated completely, allowing the output to be defined by

$$V_{LIA} \approx \frac{1}{2} V_{ref} V_I \sqrt{cos(\theta_I - \theta_{ref})^2 + sin(\theta_I - \theta_{ref})^2} = \frac{1}{2} V_{ref} V_I \tag{2.12}$$

This measurement is referred to as the quadrature component of the signal and allows the integrator output signal from Figure 2.7 to be easily be found. To minimize the influence of electrostatic actuation while maintaining sensitivity to shuttle displacement the sense voltage should be minimized and the driving frequency should be far from the ∼1 kHz natural frequency of the shuttle. In this case, a 1 Vrms sinusoidal input at 10 kHz is used as the reference waveform.

2.3.2 Actuation Capacitors

In addition to sense capacitors MIKRA incorporates a second pair of combs to facilitate calibration of the shuttle deflection and suspension stiffness. These elements have the same dimensions as the sense capacitors however there exist only 48 finger pairs. To correlate the LIA output to shuttle displacement the device must be calibrated directly using an optical microscope. Here, the shuttle is displaced using the electrostatic actuation capacitors and both the LIA voltage and separation between the heater and shuttle arms are measured. Using equation 2.7 the LIA output voltage is expected to behave linearly with shuttle position. Thus the slope of the line formed by the LIA voltage as a function of the measured gap between shuttle and heater arms defines the calibration. If the spring constant is known force magnitude can be evaluated simply using Hooke's law.

In addition to LIA signal calibration the actuation capacitors also provide the capability of dynamic tuning. Recall that the Knudsen forces achieve greatest magnitude in the transitional rarefied regime when the Knudsen number is approximately unity. Using the actuators the separation between the shuttle mass and heating element can be dynamically adjusted, shifting the location of greatest sensitivity to the desired ambient pressure. Tuning performance is not explored in the present work.

2.4 Performance Modeling

Prior to fabrication the performance of the MIKRA sensor was characterized using Simulink. The primary block diagram can be seen in Figure 2.8.

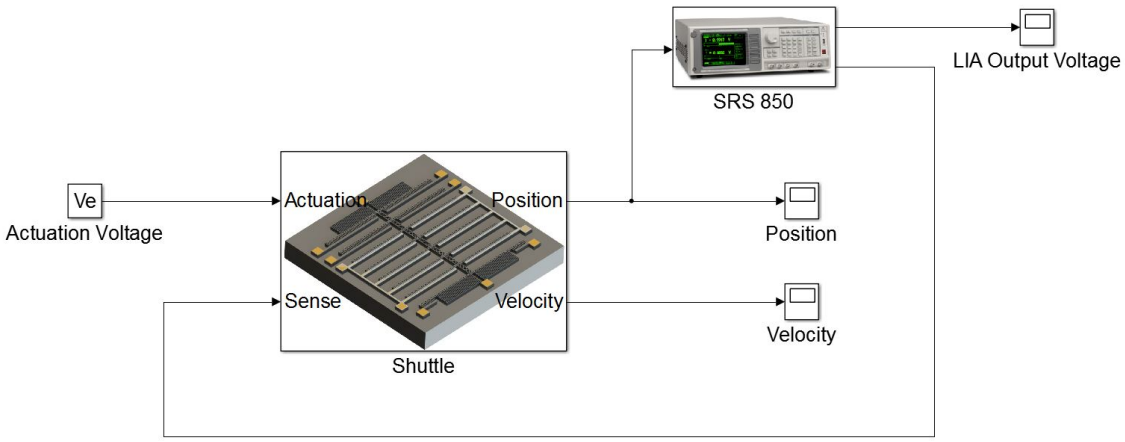

Figure 2.8. Simulink block diagram used to simulate the MIKRA device

The modeled MIKRA sensor system consists of 2 primary blocks: the “Shuttle” and the “SRS 850”. These subsystems are discussed in detail below.

2.4.1 Shuttle Modeling

The "Shuttle" block contains the force models and equations of motion used to simulate the dynamics of the shuttle mass. The free-body diagram used to define the block is shown in Figure 2.9.

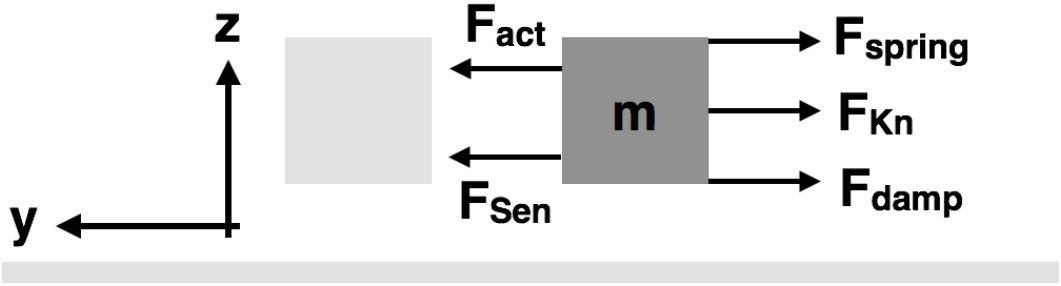

Figure 2.9. Free-body diagram of shuttle mass

Although the shuttle is permitted to displace in all three spatial dimensions, the dynamics are largely uncoupled permitting axial motion to be evaluated exclusively. Forming the appropriate equations of motion, the behavior of the shuttle mass in the axial (y-coordinate) direction can be described by

$$m\ddot{y} = -F_{Kn} - C_{damp}\dot{y} - k_y y + N_{act}\frac{\epsilon_0\epsilon_r d}{2e}V_{act}^2 + N_{sen}\frac{\epsilon_0\epsilon_r d}{2e}V_{sen}^2 \tag{2.13}$$

Here, dotted quantities refer to derivative with respect to time. The effect of Knudsen forces is implemented into the system using the model developed by Nabeth et al. [25]. In their work a correlation was developed using a 2D2V ES-BGK solver which can be used to determine the non-dimensional Knudsen force coefficient for a heated cantilever suspended over a cool substrate. The model also contains correction factors which facilitate the determination of force coefficients for arbitrary Knudsen numbers, temperature gradients, and geometries however these were not implemented as they were seen to lead to unphysical negative force quantities. Accuracy for this specific configuration has been verified through comparison to experimental measure-

ments [26]. This model is provided in equation 2.14 below. The numerically obtained constants are provided in Table B.1 of Appendix B.

$$F_{Kn} = \frac{P_\infty A(T_{heat} - T_{shtl})}{T_{shtl}} \frac{1}{A_1 Kn^{\alpha_1} + B_1 Kn^{\beta_1} + \Gamma_1 Kn^{\gamma_1}} \tag{2.14}$$

As a result of the complex nature of transitional rarefied fluid flows the influence of aerodynamic damping must also be evaluated using a numerically computed empirical correlation. This effect was incorporated into the system model using a correlation presented by Guo and Alexeenko whereby the squeeze-film damping force on a microcantilever near a substrate was investigated using quasi-steady 2D2V ES-BGK solver [13]. The damping force from this model is shown in equation 2.15. Numerically computed constants are provided in Table B.2 of Appendix B.

$$C_{damp} = \frac{A_2(d/g)^{\alpha_2}}{1 + B_2(d/g)^{\beta_2} Kn(d/g)^{\gamma_2}} A \tag{2.15}$$

2.4.2 Lock-In Amplifier Modeling

The "SRS 850" block contains the model used to describe the behavior of the LIA. The block receives the position output from the "Shuttle" block and computes the corresponding fringeless capacitance. Theoretical integrator output voltage is then obtained from equation 2.7. This output, in turn, is multiplied by both the reference waveform and its phase shifted component, filtered, and its quadrature value computed. A 1 Vrms LIA reference signal at 10 kHz is used as the input voltage to the sense capacitors within the "Shuttle" block in order to both minimize the effects of electrostatic actuation and preserve sensitivity.

2.4.3 Simulation Results

The initial conditions for arm gap and velocity were set to 20 μm and 0 m/s respectively. An arbitrary chamber pressure of 300 Pa is simulated so as to illustrate

typical shuttle and LIA responses. Ode45 is used as the numerical solver. To account for the large accelerations of the shuttle the initial time step size was chosen to be 1e-6 s. The total simulation time was set to 5 s. The results of shuttle displacement and LIA output are provided in Figure 2.10. Figure 2.10(b) details the point of heater engagement.

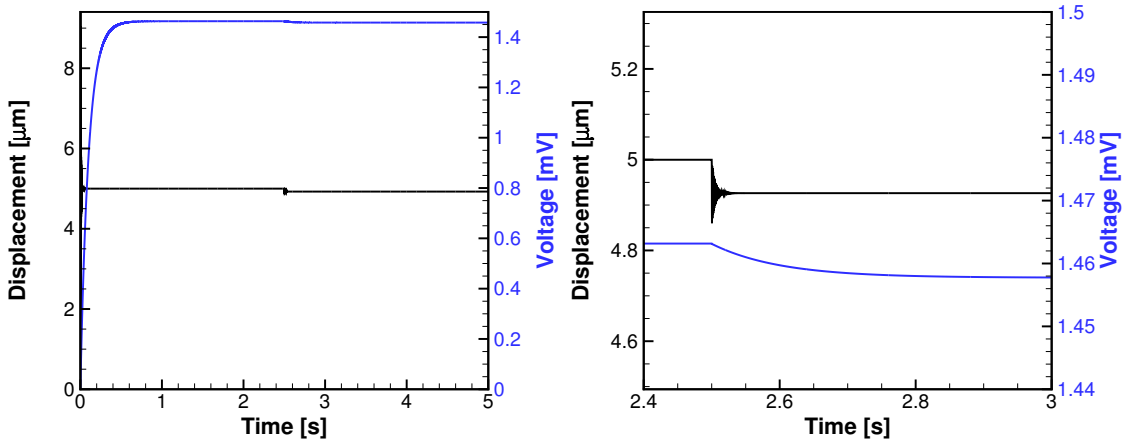

(a) Displacement and LIA output voltage over entire simulation period

(b) Displacement and LIA output voltage after heating element engagement

Figure 2.10. Simulation results for device having 600 μm spring flexure length

At the beginning of the simulation the heating elements are deactivated. Bias is applied to the actuation capacitors and the shuttle displaces 5 μm to its new equilibrium position. As expected, this decrease in arm separation corresponds to an increase in capacitance and ultimately an increase in LIA output voltage. At 2.5 s current is supplied to the heating elements and the shuttle begins to displace away from the heater arms under the influence of Knudsen forces. After a period of time the shuttle reaches a steady state whereby the Knudsen forces are in equilibrium with the restorative force from the serpentine suspension. At this point the temperatures of the heating elements, shuttle arms, and ambient air are 80, 24, and 24 °C respectively. These temperatures were assumed as the heat transfer coupling between the gas and the shuttle arm in the rarefied fluid is difficult to obtain. Studies on microscale heat

transfer in rarefied flows suggest these assumptions are reasonable [19, 11]. Taking the change in LIA output before and after heater engagement provides a measure of shuttle deflection due only to Knudsen forces since, according to equation 2.5, the actuation mechanism is independent of stroke length. Although the changes in capacitor output voltage are small, these simulated results demonstrate the feasibility of the sensing concept for shuttle displacement quantification as LIAs are able to resolve amplitude changes as low as 100 nV.

Experimentally, deflection magnitude can be evaluated directly from the LIA voltage through calibration against a series of measured displacements. These measurements, in turn, can be used with a second calibration for suspension stiffness to provide an estimate of force magnitude. Evaluation of these quantities is primarily of theoretical interest and is not necessary for the purpose of gas-property sensing however.

3. MIKRA FABRICATION

The MIKRA sensor was fabricated in the SciFres Nanofabrication Laboratory in Discovery Park's Birck Nanotechnology Center at Purdue University. Fabrication began using a silicon-on-insulator wafer having nominal handle, box, and device thicknesses of 400, 4, and 50 μm respectively. Device and handle layer resistivities were identical at 0.005-0.02 $\Omega\dot{c}m$.The wafer was initially cleaved into 4 equally sized quadrants using a diamond scribe. Not only does this technique better facilitate sampling handling throughout the fabrication process but also reduces process costs by both reducing the number of required photomasks from 4 to 1 as well as minimizing sample losses in the event of accidental damage. The overall fabrication flow is shown in Figure 3.1. The complete fabrication recipe with accompanying notes can be found in Appendix B.

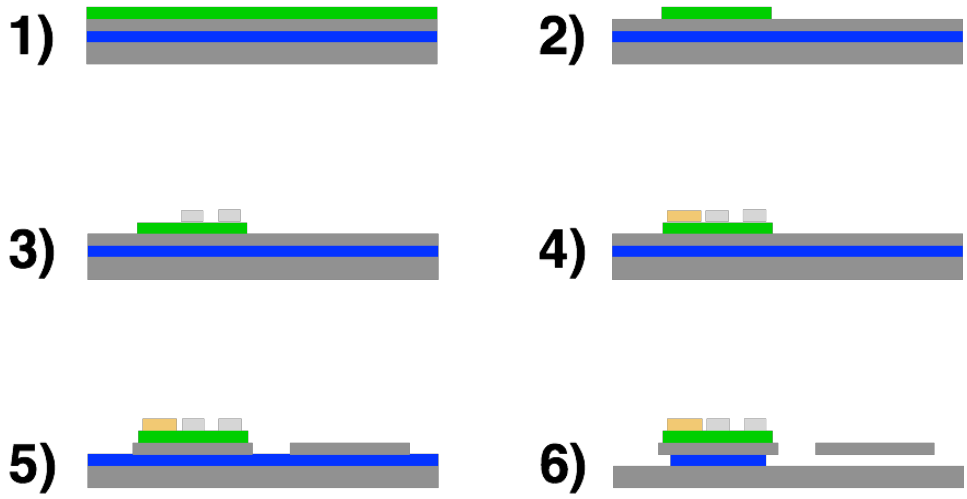

Figure 3.1. MIKRA fabrication flow

Step 1: LPCVD Silicon Nitride Deposition

A 296 nm thick layer of low-pressure chemical vapor deposition silicon nitride is thermally grown on the wafer sections in a Protemp horizontal furnace to serve as an electrical insulating layer between the platinum heating elements and the silicon heater arms. Silicon nitride was selected due to its desirable electrical insulating properties and chemical resistance to hydrofluoric acid needed during sacrificial oxide etching. Film thickness is verified directly using a Filmetrics thin film measurement system.

Step 2: Silicon Nitride Patterning and Etch

During the LPCVD process the wafer sections acquire a uniform nitride layer over the entire surface. Therefore, before patterning of the nitride on the device layer the unwanted film on the handle wafer is first removed using a Panasonic E620 plasma etching system. This process is necessary to permit the formation of a low resistance electrical connection between the chip carrier and the substrate.

As a result of the high aspect ratio features of MIKRA high quality photoresist adhesion is difficult to achieve. To improve adhesion properties hexamethyldisilizane is spin coated onto the silicon nitride surface prior to PR application. Immediately following HMDS application the wafer is spin coated with AZ 9260 PR at 3500 rpm for 30 seconds using 5 second acceleration and deceleration ramps.

After PR spin coating the wafer is placed on hot plate and "soft baked" to remove the solvent material. The baking process allows the polymer to form a hard protective coating on the wafer surface but also liberates water from the film. To improve patterning performance a 30 minute rehydration period is required before further processing.

With the sample rehydrated the wafer is placed into a Suss MA-6 mask aligner whereby it is exposed under ultraviolet light at a flux intensity of 14 W/cm^2 for 80 seconds. The sample is then agitated manually in a 3:1 DI H_2O : AZ400K developing

solution for approximately 1.3 minutes. The etch rate was seen to vary between processes, altering the developing time by up to 30 seconds. Completion of the development step must therefore be verified using a microscope. The PR is hard baked after development to increase its resistance to the harsh plasma environment used during the removal of the silicon nitride.

Similar to the handle wafer, the insulating silicon nitride film on the device layer is etched using the Panasonic E620. The total required etch time is 3.25 minutes. It is important to note that the etch chemistry used to remove silicon nitride is fluorine-based and tends also to etch silicon aggressively. To prevent unwanted overetching a fluoropolymer such as C_4F_8 is often introduced as a passivation layer in between etch cycles. This technique was not implemented however as it was found to lead to unwanted polymer buildup on a test sample during recipe characterization.

Step 3: Heating Element Patterning and Liftoff

With the silicon nitride insulation patterned the PR material is removed using Baker PRS2000 at 90°C followed by a 3:1 H_2SO_4 : H_2O_2 piranha solution. The heating elements are patterned with HMDS and AZ 9260 using the same recipe as that used for the silicon nitride layer with the exception of the hard bake step. As a result of the inherent difficulty associated with the etching of platinum a lift-off process is employed to pattern the filaments. This technique uses the PR itself as a sacrificial layer allowing the platinum material to be "lifted off" of the coated areas. Metallization is performed in an Airco e-beam evaporator. A 10 nm chromium adhesion layer is first deposited followed by 100 nm of platinum filament material. Chromium was chosen over the more common titanium due to its superior resistance to hydrofluoric acid. Following evaporation the sample is placed in another heated PRS2000 solution and allowed to soak overnight. This extended bath ensures the sacrificial PR material is completely dissolved. The wafer is then briefly placed in an ultrasonic bath to remove

excess material and subsequently cleaned in Nanostrip in preparation for additional metallization.

Step 4: Wire Bond Pad Patterning and Liftoff

Gold wire bonds are used to interface the macroscopic electronics with the sensor elements. To acquire adhesion the wire bonds must be welded to pads of a suitable material, in this case, gold. To form the pads HMDS and AZ 9260 are once again spun onto the clean wafer, exposed, and developed using the same lithography process as that for the heating elements. The lithography process is proceeded by the evaporation of a 10 nm chromium adhesion layer followed by a 30 nm layer of gold. The bond pad patterns are subsequently lifted off in PRS2000 using the same process as that used for the heating elements.

Step 5: Device Layer Patterning and Etch

The final step in the primary fabrication involves the formation of the silicon structures. The elements are pattered using the lithography recipe described above including the hard bake. Caution must be observed when hard baking the high aspect ratio structures of the device layer as PR flow can occur and potentially lead to deformed features. Following lithography the wafer is mounted to a silicon backing or support wafer using crystal bond compound. This step is necessary for installation into the etching equipment. Etching is performed in Surface Technology Systems Advanced Silicon Etch plasma etcher using standard Bosch process chemistry. As a result of the high aspect ratio structures the chamber pressure is lowered after several etch cycles in order to permit deeper ion penetration and greater etch uniformity. Following the etch the samples are coated with a thick protective layer of aerosol-based AZ 9260 in preparation for dicing in a Disco DAD200 saw.

Step 6: Oxide Removal and Device Release

The final step in the overall fabrication of the MIKRA sensor involves the etching of the sacrificial thermal oxide layer. Removal of the oxide releases the shuttle, allowing it to actuate in response to Knudsen and electrostatic forces. This process must be performed carefully as accidental shuttle contact with the substrate surface can lead to permanent stiction and device failure.

To prevent stiction many modern MEMS devices are released using HF vapor. During characterization it was found that vapor phase HF aggressively attacked the LPCVD nitride, undercutting the heaters and rendering them unusable. For this reason the release process was performed in a 49% aqueous HF solution, requiring roughly 14 minutes to achieve complete undercut of the movable structures.

After etching the samples are immediately cycled through several DI water baths to remove them from the aggressive HF solution. Samples are transferred between baths by means of a ladle to prevent exposure to air and potential stiction. Following the DI rinse the devices are cycled through another series of baths containing isopropanol in preparation for drying. Release is performed in a Tousimis Automegasamdri critical point dryer using supercritical CO_2. In this process the samples are initially enclosed in a pressure vessel containing only pure IPA. Liquid CO_2 is then flushed through the system until the IPA is completely removed. Following the flush the pressure and temperature are increased to the critical point and maintained for a fixed duration. Pressure is subsequently returned to atmospheric pressure allowing the CO_2 to escape in gaseous phase. The result is a dry and released sample free of stiction. An image of a sample after this process is shown in Figure 3.2.

Following fabrication the samples are cleaned in oxygen plasma then attached to 24-pin leadless chip carriers which have been previously soldered onto custom PCBs having male header pins. Sample bonding is performed using electrically conductive epoxy to permit substrate grounding. After curing the mounted devices are then wire

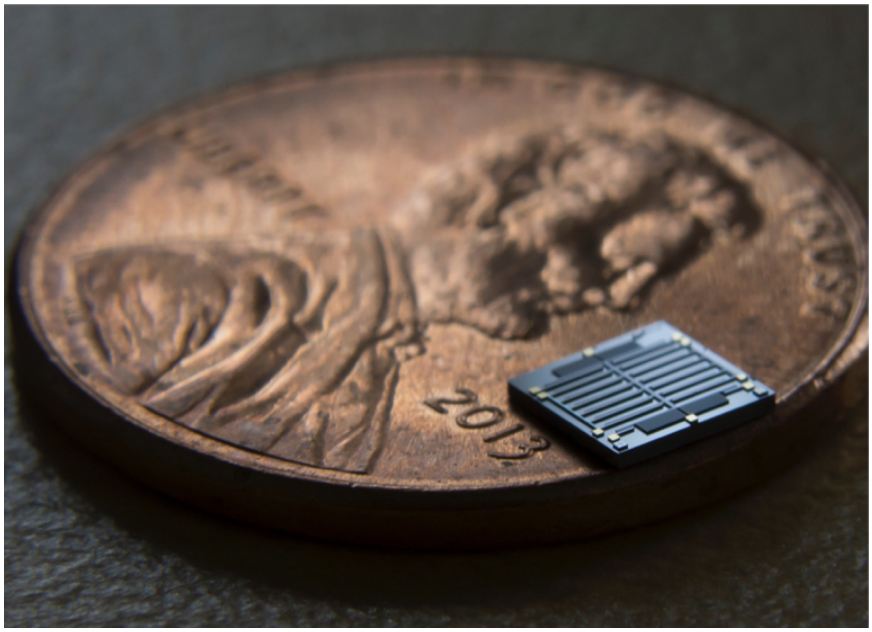

Figure 3.2. Completed MIKRA sample shown on penny for scale

bonded to the LCC and installed into the experimental apparatus, completing the fabrication.

An SEM image of a completed and packaged MIKRA device with labeled components and dimensions is shown in Figure 3.3. The experimental setup used for the characterization of MIKRA is described in the following chapter.

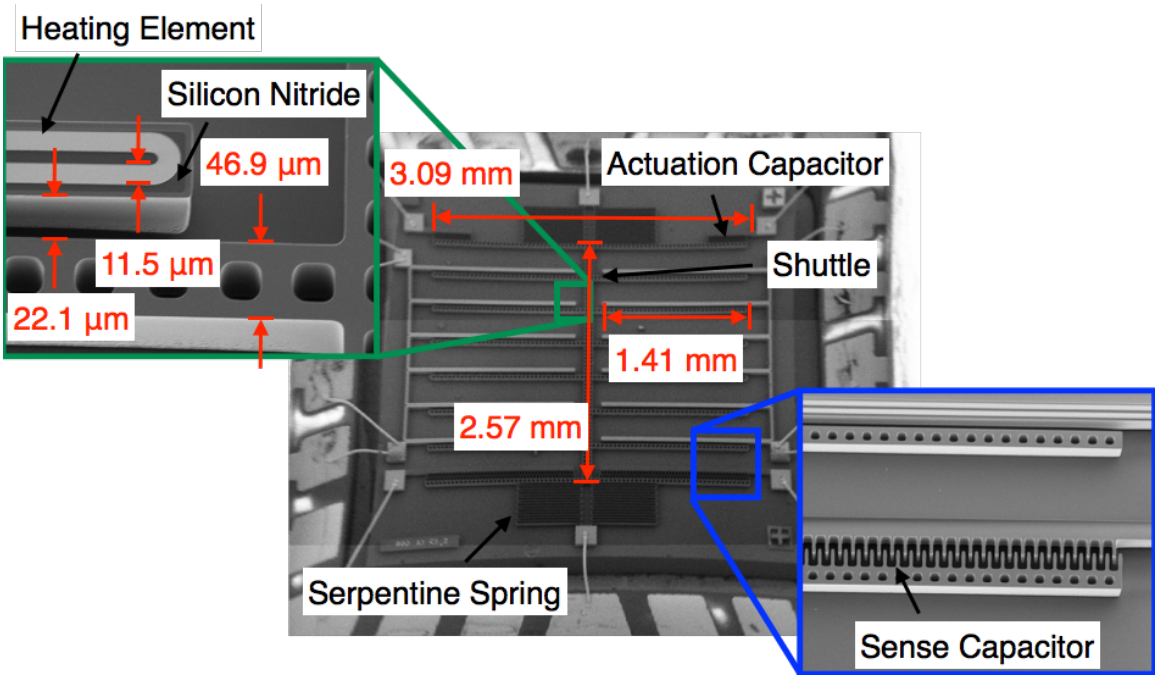

Figure 3.3. SEM image of package MIKRA device with labeled components and dimensions

4. EXPERIMENTAL SETUP

The experimental setup used for the testing and characterization of the MIKRA device is shown in Figure 4.1.

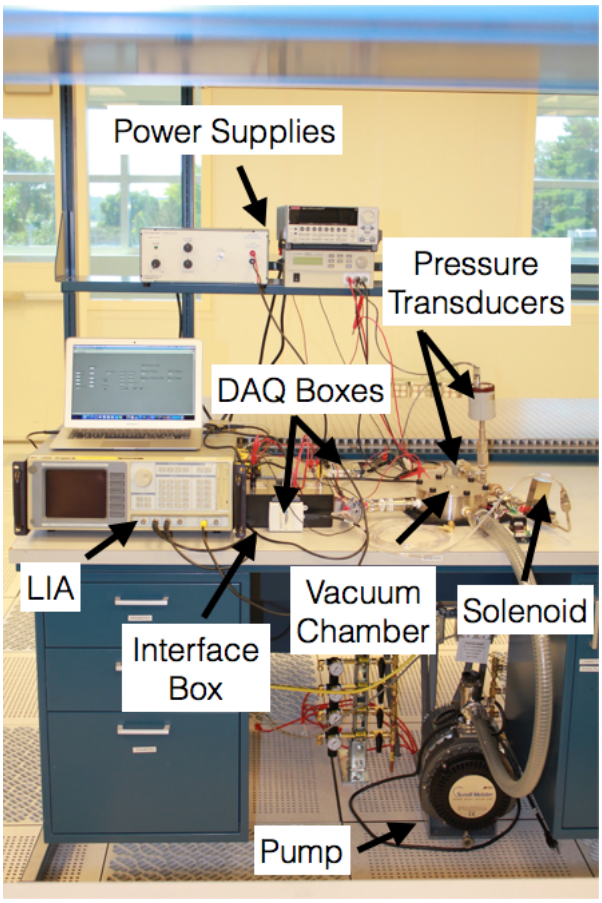

Figure 4.1. Experimental setup use for characterization of MIKRA

All software and hardware control is performed using the National Instruments LabVIEW graphical programming language. Heating element data acquisition is performed by a NI 12-bit USB 6008 DAQ system whereas the pressure and LIA measurements are collected with a higher resolution NI 24-bit USB 9239. Analog

control voltage output for the heating elements is carried out using the USB 6008 whereas control output for pressure regulation is performed using an Arduino with a DC motor driver shield.

The MIKRA sensor is located inside of a custom machined 4.3 cm^3 stainless steel vacuum chamber. The vacuum is driven by an Inest-Iwata dry scroll pump having an ultimate pressure of approximately 1.8 Pa. A dry pump was selected to prevent the back streaming of mineral oil into the chamber which could potentially damage the sample or corrupt the measurements. To prevent damage to the pump as a result of gas loading a throttling valve is attached at the inlet downstream of the chamber. This valve chokes the flow entering the pump, decreasing gas load and greatly extending the permissible pressure range of the vacuum chamber. The throttle valve is also used to set the mass flow rate through the chamber at lower pressures by defining the minimum aperture in the system.

4.1 Vacuum Chamber

The vacuum chamber contains a total of 4 feedthrough ports accommodating 1/2" male pipe thread fittings. An image of the chamber interior with signal conditioning electronics is shown in Figure 4.2.

Feedthrough 1 is a 10-pin electrical interface which connects the heating elements, LIA signal conditioning circuitry, and actuation capacitors to the interface box. Feedthrough 2 connects the chamber to the scroll pump. Feedthrough 3 connects to plumbing which interfaces to the pressure transducers and chamber gas input line. Finally, feedthrough 4 is used exclusively as an input for the LIA reference waveform. All electrical hardware is referenced to the vacuum chamber which is maintained at an earth ground potential. Integrated into the lid is a CaF window which is nearly transparent to the infrared spectrum. This feature permits the direct measurement of device temperature distribution using a thermal microscope. The chamber contains a step cut intended for the installation of custom circuit boards. The board from

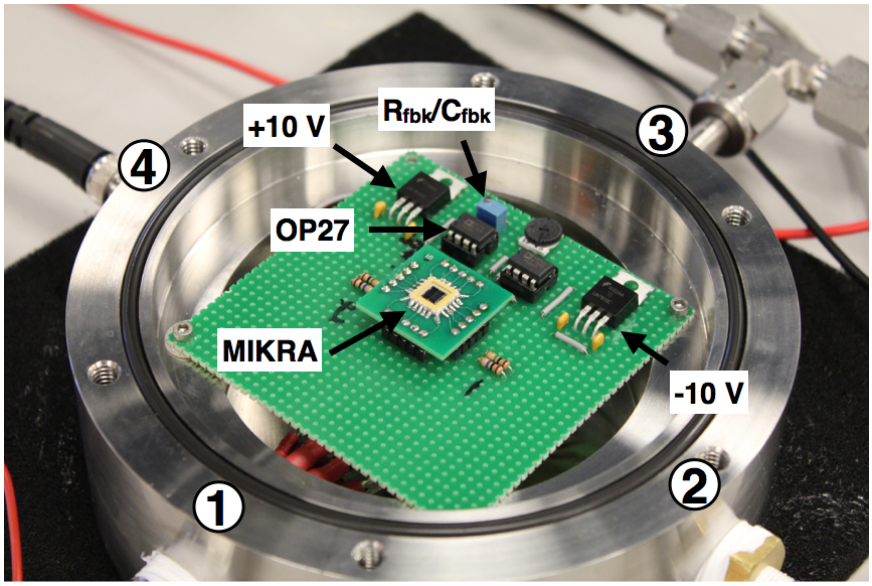

Figure 4.2. Vacuum chamber used for the characterization of MIKRA

Figure 4.2 contains the integrator circuit hardware described in Figure 2.7 as well as the heating element voltage dividers which are described below.

4.2 Pressure Measurement and Regulation

Chamber pressure is measured using a 10 Torr full-scale MKS 626B Baratron for values below 1250 Pa and a MKS 902B for values above. Data acquisition for both transducers is performed using the USB 9239. A software-based PI controller is employed for regulation. The controller receives the error between the measured pressure and the user-defined setpoint, outputting a corresponding analog voltage to the base of a 2N2222 NPN transistor. The transistor's collector is connected to the solenoid valve of a mass flow controller in series with a current limiting resistor and 15 Volt supply rail. The emitter is at ground potential. The small current output from the PI controller is thus used to control a large load across a solenoid, allowing chamber pressure to be precisely regulated.

4.3 Capacitance Measurement

Capacitive sensing is carried out with the aid of a Stanford Research Systems 850 LIA. The operating parameters used in all tests are provided in Table 4.1.

Table 4.1. LIA parameters used in Knudsen force measurements

Parameter	**Value**	**Unit**
Reference Amplitude	1	V_{RMS}
Reference Frequency	10	kHz
Sensitivity	100	mV
Filter Time Constant	10	ms
Low Pass Filter Cutoff	24	dB/oct
Dynamic Reserve	0	dB
Coupling	AC	
Line Filters	60,120	Hz
Grounding	Float	

The reference signal from the LIA is connected to feedthrough 4 via a BNC cable. A reference frequency of 10 kHz was selected such that it is far from the natural frequency of the sensor yet below the corner frequency of the OP27 op-amp. This waveform drives the sense capacitors on the MIKRA device in parallel, leading to a total capacitance value of their sum. The output from the integrator circuit is passed through feedthrough 1 into the interface box. The signal is then fed back into the LIA where the DC component is extracted by the process described in equations 2.8 through 2.12. The amplified analog output from the LIA corresponding to this DC signal is measured by the USB 9239.

4.4 Heating Elements and Interface Box

The interface box serves as the central bus for the experimental apparatus. An image of the front panel is provided in Figure 4.3. The use of the box facilitates a modular system, allowing the setup to be easily moved.

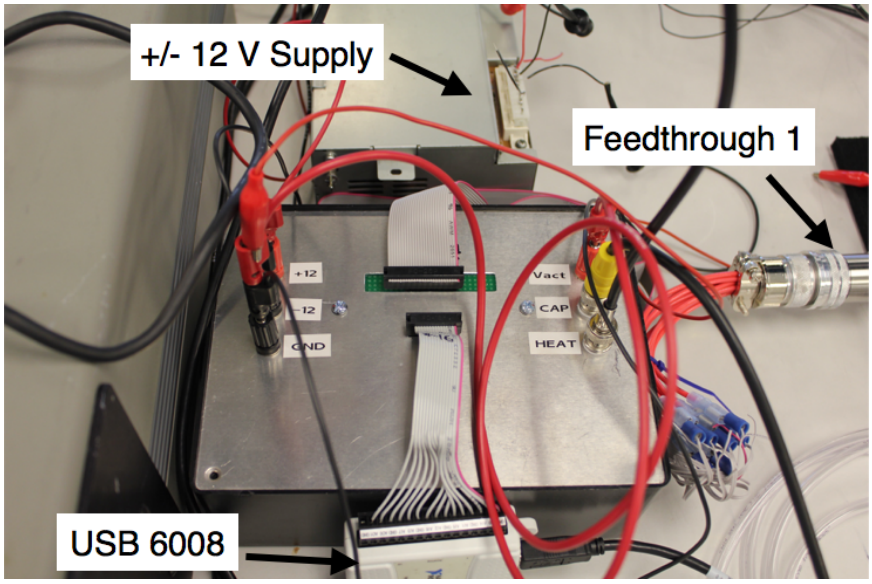

Figure 4.3. Interface box for power supplies, heating elements, and LIA signal

The front panel houses connections linking various system elements to their respective DC power supplies. The ground connection is tied directly to the chamber and earth reference. The panel also contains a series of pin headers and a terminal block to easily interface the heating elements with the USB 6008. The cascaded NPN/PNP amplifier used to drive the heating elements is located inside of the box.

Similar to chamber pressure, the power applied to MIKRA's heating elements is regulated using software-based PI controllers. The controller drives the analog outputs of the USB 6008 which connect to the cascaded NPN/PNP transistor amplifiers as shown in Figure 2.5. From the figure, both the voltage drop across the heating elements as well as the common mode of the shunts are larger than the permissible ± 10 V input voltage of the USB 6008, necessitating the use of a pair of voltage di-

viders across each of the shunts. The first divider is located within the interface box and the second is on the circuit board in the vacuum chamber. The output voltage across the voltage dividers can be described by

$$V_{out} = \frac{R_2}{R_1 + R_2} V_{in} \tag{4.1}$$

The use of voltage dividers provides an alternate path to ground for the current flowing through the shunts and heaters. The resistances from equation 4.1 should therefore be large relative to the load resistance, minimizing leakage. In the MIKRA setup R_1 was taken as 10 MΩ and R_2 as 1 MΩ, leading to a nominal divider ratio of 11.

The large impedance across the voltage dividers greatly exceeds the 100 kΩ input impedance of the USB 6008, forcing the DAQ unit to serve as a current sink. To eliminate this error a unity-gain buffer formed by an LM358 is placed between the divider and USB 6008, converting the high-impedance divider load to a low-impedance output. The divider ratios were acquired experimentally by simultaneously measuring the true voltage with a GΩ impedance meter and divider voltages with the USB 6008. The results are provided in Table 4.2.

Table 4.2. Voltage divider ratios for heating elements and shunt resistors

Parameter	Value
Heater 1	10.96
Heater 2	11.15
Shunt 1	11.67
Shunt 2	9.86

In addition to the cascaded amplifier the unity-gain buffer circuits are also located inside of the interface box.

4.5 Test Procedure for Knudsen Force Quantification

Prior to testing the pump is activated and the system is allowed to outgas for roughly 30 minutes. This period also provides the signal conditioning and pressure transducer electronics sufficient time to warm up. After the outgassing interval the user-defined test parameters are input into the LabVIEW program. A summary of these parameters used in all Knudsen force measurements is provided in Table 4.3.

Table 4.3. Test parameters used in Knudsen force quantification tests

Parameter	Value	Unit
Initial Pressure	10	Pa
Final Pressure	15000	Pa
Number of Pressures	16	
Interval Time	5	min.
Delay Time	5	min.
Heater 1 Power	75, 100, or 125	mW
Heater 2 Power	75, 100, or 125	mW
Heater On Time	5	sec.
Heater Off Time	55	sec.

With the input parameters defined pressure tracking is initiated and the program is allowed to reach the first setpoint. Using the specified upper and lower bounds on chamber pressure the program calculates all following intermediate pressures by means of a logarithmic distribution. These pressures serve as the PI controller set-points throughout the duration of testing. After the chamber pressure stabilizes around the first setpoint automatic logging is initiated and the test sequence begins. From this point forward all test and data logging processes are automated. This sequencing follows the test procedure outlined in Figure 4.4.

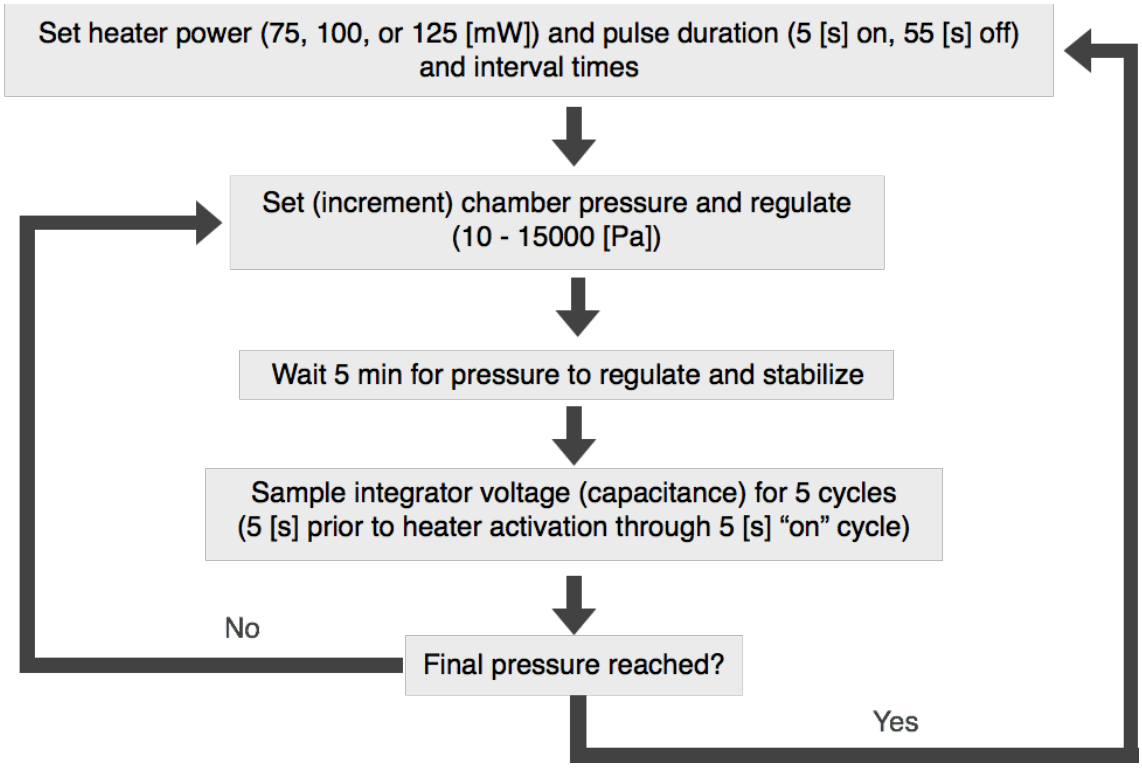

Figure 4.4. Automated test procedure for Knudsen force quantification tests

To maintain a large thermal gradient and prevent thermal spreading the heating elements are pulsed on for 5 seconds and off for 55 seconds (12% duty cycle). During the heating phase the heaters are individually regulated by their respective controllers at the specified power (75, 100, or 125 mW) using the measured current and voltage. The heating and cooling cycling is performed a total of 5 times for each pressure setpoint. The sense capacitors are sampled 5 seconds prior to the heating cycle in addition to the cycle itself. Sampling in this way allows only the relative change in capacitance to be considered, minimizing the potential for measurement errors over time due to drift.

Following the 5 measurement cycles (5 minute interval time) the pressure setpoint is advanced and the chamber is allowed to stabilize for 5 minutes (delay time) before initiating the next sequence of measurements. The process is repeated until the final

pressure setpoint is achieved. At this point the experimental setup is powered down and the data is post-processed.

4.6 Test Procedure for Thermal Mapping

To evaluate the temperature distribution of the MIKRA sensor under the application of heater power the sensor and vacuum chamber assembly is placed under a QFI Infrascope thermal imaging microscope. The test procedure is similar to that for the measurement of Knudsen forces however both the heater engagement and pressure advancement are performed manually to synchronize with the camera.

At the beginning of the test pressure tracking is initiated and the system is allowed to settle around the specified initial pressure The distribution of setpoints is carried out in the same manner as before. Following stabilization the heaters are activated and the first heating and cooling cycle is allowed to execute. During the last 5 seconds of the 1^{st} 1-minute heating a cooling cycle the thermal microscope begins acquiring images. A total of 300 frames are collected at a rate of 10 Hz, totaling 30 seconds of sampling. After the sampling period the heating elements are disengaged and the pressure is manually advanced to the next setpoint. The process is repeated until all pressure setpoints have been imaged. Performing measurements in this way allows the transient temperature distribution of the entire MIKRA sensor to be evaluated, providing deeper insight into the thermal properties of the device and their dependence on applied power and chamber pressure.

5. DISPLACEMENT AND SPRING CONSTANT CALIBRATIONS

According to equations 2.7 and 2.12 the shuttle displacement due to Knudsen forces can be inferred directly from the LIA output. As a result of the inherently small capacitances associated with the microdevice (∼250 fF) the combined parasitic capacitances from the vacuum chamber, vias, bond wires, etc., are on the order of picoFarads, prohibiting accurate determination of an absolute position measurement without calibration.

5.1 Calibration of Shuttle Displacement

The capacitive measurement as obtained from the LIA is calibrated to deflection with the aid of the actuation capacitors. To perform this calibration the experimental apparatus is located beneath a Leica DCM8 confocal microscope. A 20x magnification objective is used to capture the position of the shuttle. Starting from ground potential the voltage across the actuation capacitors was increased in increments of 10 V to a final value of 40 V. This ultimate voltage was selected to minimize the potential for transverse pull-in, an effect which has been observed in several devices. Ideally, the symmetry of the comb structure prevents this behavior however the large suspension compliance in combination will minor offsets within the comb system due to internal stresses of the silicon or structural nonuniformities lead to this undesirable effect. The response from the LIA to the input voltage is illustrated in Figure 5.1.

At each actuation voltage an image of the actuation capacitors was captured and manually analyzed using ImageJ. The relative change in separation between the fixed comb arm was measured directly from the image, allowing the displacement to be inferred from the LIA output voltage by means of a linear least-squares fit. The

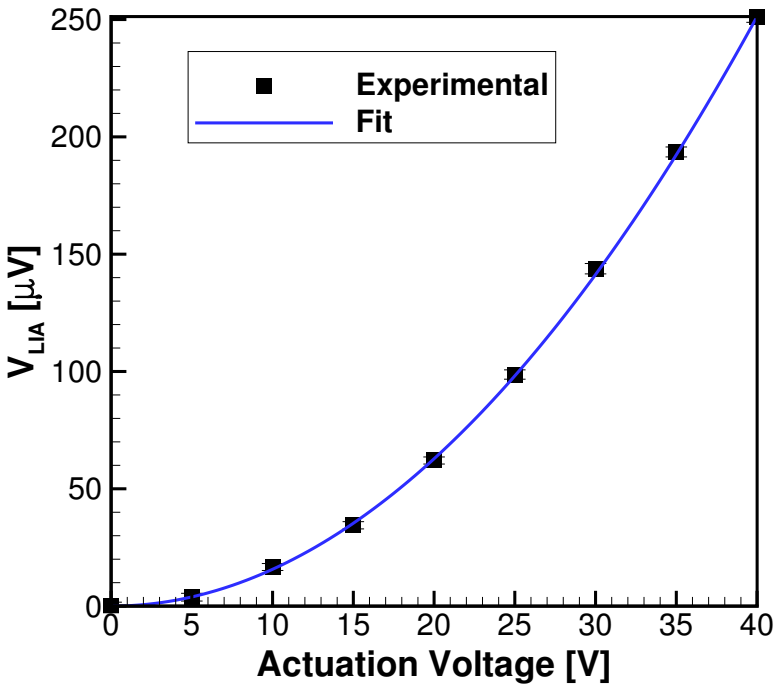

Figure 5.1. LIA output voltage as a function of actuation voltage

measured relative shuttle displacement from the grounded state for actuation voltages of 0, 20, 30, and 40 Volts as a function of LIA output voltage is shown in Figure 5.2.

As a result of the focal length limitations imposed by the lenses of the microscope the 20x magnification objective offered the highest achievable spatial resolution. This constraint leads to a systematic calibration uncertainty of around 30% due to the difficulty in resolving sub-micron length scales. Nevertheless, the calibration results in a variation of 182.4 m/V with corresponding R^2 value of 0.999, indicating the variation is linear as expected.

5.1.1 Calibration of Suspension Spring Constant

To determine Knudsen force magnitude from the shuttle displacement measurements the spring constant of the shuttle suspension must be known. Originally, the

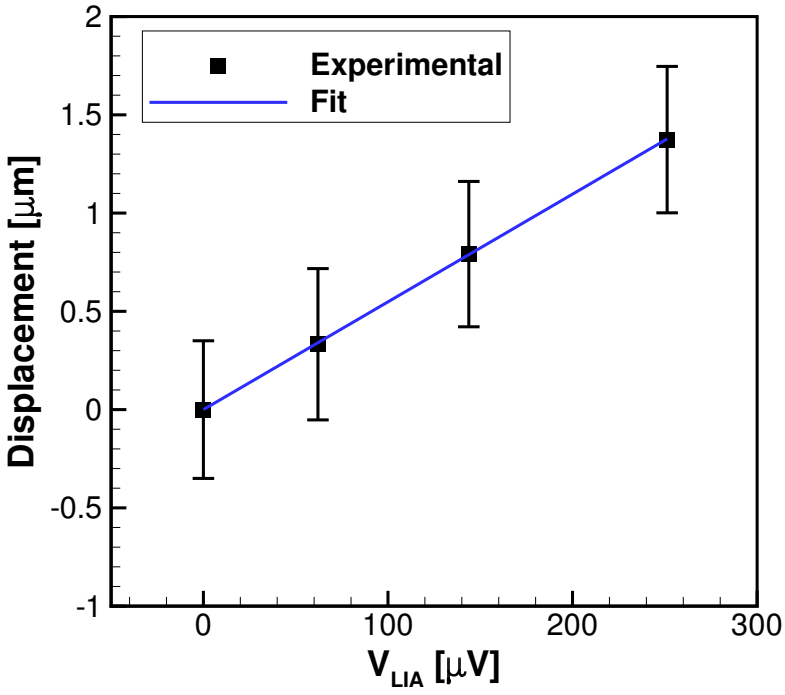

Figure 5.2. LIA output voltage as a function of shuttle displacement

calibration procedure was to be carried out by evacuating the vacuum chamber and measuring the resulting undamped natural frequency of the shuttle system by means of a spectral analysis of the sense capacitor signal. Assuming the volume of the shuttle can be measured and the density of the silicon device layer is known the computation of spring constant using this technique is straightforward. Unfortunately, from the theoretical estimate of the spring constant the expected resonant frequency is around 1 kHz, far beyond the highest corner frequency of the LIA's built-in lowpass filters.

To find the spring constant a somewhat crude assumption must be made regarding the nature of the capacitance of the comb assembly. Recall from equation 2.5 that for a comb capacitor the actuation force is dependent on the product of a capacitive constant and the square of the bias voltage. Additionally, from the finite element analysis of the suspension assembly it was determined that the serpentine springs obey Hooke's law, allowing the shuttle displacement to be written as

$$F_{act} = k_y \frac{V_{LIA}}{\Lambda_{LIA,y}} = N_{act} \frac{\epsilon_0 \epsilon_r d}{2e} V_{act}^2 \implies V_{LIA} = \frac{\beta \Lambda_{LIA,y}}{k_y} V_{act}^2 = p V_{act}^2 \qquad (5.1)$$

Using equation 5.1, $\beta\Lambda_{LIA,y}/k_y$ can be determined by means of a quadratic least-squares fit of the measured LIA output and actuation voltages from Figure 5.1. Using this fitting parameter and neglecting the influence of fringe fields near the edges of the combs the spring constant can be evaluated simply by using the measured device dimensions and displacement calibration. These parameters are listed in Table 5.1.

Table 5.1. Parameters used for spring constant calibration

Parameter	Value	Unit
N_{act}	48	
ϵ_0	8.854×10^{-12}	A^2s^4/m^3kg
ϵ_r	1.0	
d	50	μm
e	5	μm
$\Lambda_{LIA,y}$	182.41	V/m
p	1.570×10^{-7}	N/V^2

Using the data from the table above the spring constant is found to be 2.47 N/m, around 18% of that predicted by the finite element model. Using this calibrated value and assuming a nominal shuttle mass of 0.157 μg, the natural frequency is estimated to be 632 Hz. Thus, the frequency of the reference waveform of 10 kHz is sufficiently high so as not to appreciably disturb the position of the shuttle during the measurement. Although there inevitably exists some error in the calibration due to both the idealized fringeless capacitor assumption and uncertainties in measured displacement, a spring constant lower than theoretically predicted can be expected by considering the fabrication. The measured flexure and meander widths are 7.79 μm, 78% of the nominal dimension. Considering the effect of beam width on spring

constant from equation 2.1 it can be seen that the spring constant varies with the cube of this parameter. Thus, using the measured width the spring constant will assume a value around 47% of that which was designed. Additionally, it should be noted that the silicon structures which define the MIKRA geometry are formed using deep reactive ion etching. This technique employs alternate cycles of chemical etching and passivation to form high aspect ratio structures such as those comprising the suspension elements. The etch process is highly sensitive to a number of etch parameters including chamber pressure, gas mixture ratios, RF power, and bias voltage, leading to undesirable reentrant or retrograde profiles if not precisely tuned. Capturing SEM images of the MIKRA sensor following the etch process it was found that the etch profile was slightly reentrant, leading to structures which become thinner as the etch progresses. This effect also likely contributes to the lower spring constant however the impact has not been quantified.

6. THERMAL IMAGING AND ANALYSIS

The temperature distribution of the MIKRA device is measured under the application of constant heater power for a range of logarithmically distributed pressures between 10 Pa and 15 kPa. Heater power settings of 100, and 125 mW are tested over a total of 9 pressure setpoints. Measurements at an applied power of 75 mW were also collected however these results have been omitted due to a suspected malfunction in the test apparatus during the test sequence. As a result of the small view field of the 20x thermal microscope objective lens each test is performed twice, once for each heating element. A thermal image for heater 1 under an applied power of 100 mW and pressure setpoint of 10 Pa in Figure 6.1.

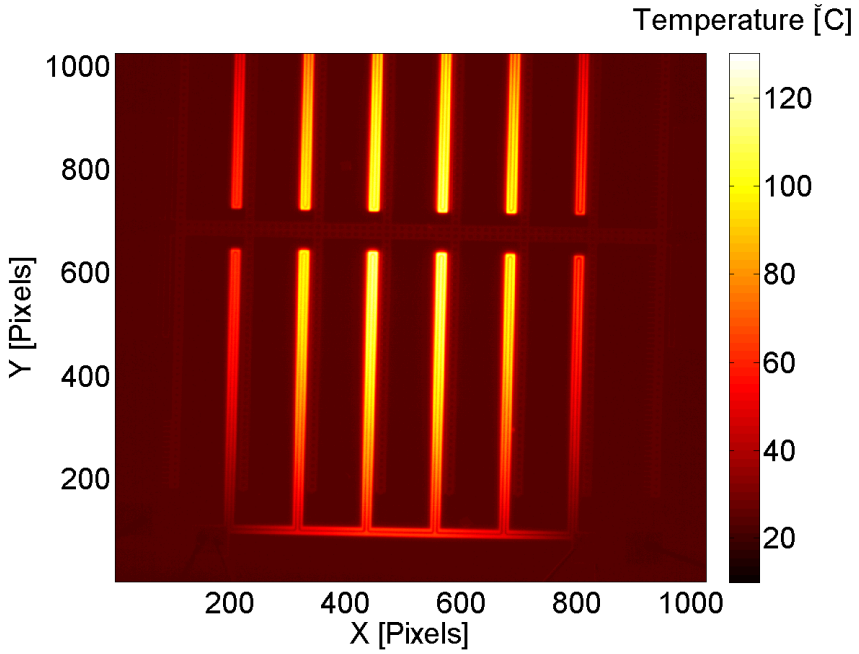

Figure 6.1. Temperature map for heater 1 at 100 mW in air at 10 Pa

Clearly, the temperature distribution along the heater arms is nonuniform along the wetted length, exhibiting the highest temperature at the free end. Similar to wet area, the wet length refers to the length of the heater arm directly exposed to the shuttle arm. In addition to the axial non-uniformity there also exist variations in temperature distribution between the arms themselves making the accurate quantification of overall temperature difficult. This behavior is consistent with the temperature maps obtained at higher pressures however the thermal gradient itself is of lower magnitude.

6.1 Variation of Average Heating Element Temperature with Ambient Pressure

Taking the average temperature along the wet length of each of the heater arms as well as the corresponding shuttle arms the variations with pressure at both 100 mW and 125 mW are presented in Figures 6.2(a) and 6.2(b) respectively. The substrate temperature is obtained using the same extraction profile, displaced to a location adjacent to the shuttle arm on the opposite side of its gap-facing surface.

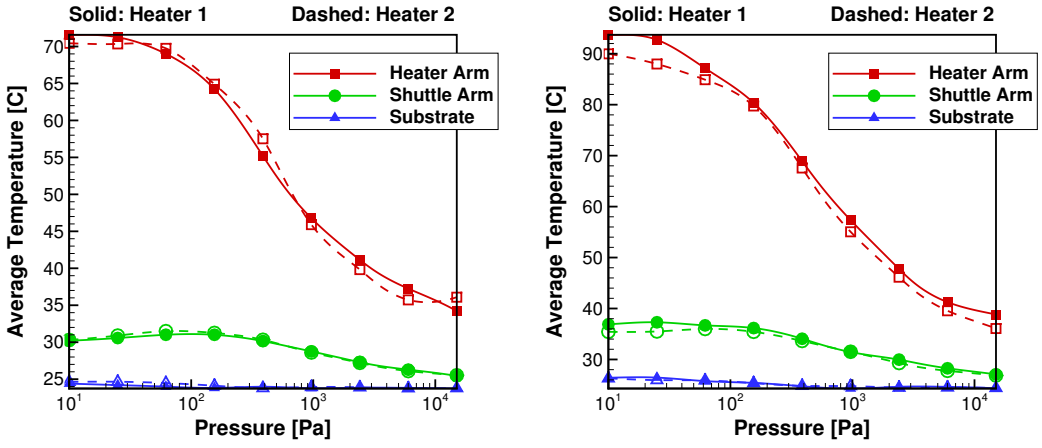

(a) Power = 100 mW

(b) Power = 125 mW

Figure 6.2. Average heater arm, shuttle arm, and substrate temperatures

Due to the reduced efficacy of convective and conductive dissipation, the variation in temperature between the heater and shuttle arms is greatest at low pressures. Substrate temperature can be assumed constant over the entire range of pressures, showing a variation of only around 6% from the average. The shuttle temperature is seen to vary non-monotonically with pressure, achieving maximum value at around 150 Pa in both cases. This behavior can be explained by considering the balance between heater arm temperature and the thermal dissipation to the fluid. The increased collision frequency of the molecules with increasing pressure leads to an increase in heat flux to the gas, resulting in a decrease in heating element temperature. This enhancement, in turn, also leads to a corresponding increase in net flux from the heater arm to the shuttle arm. A balance is therefore struck between heater arm temperature and the gas capacity to transfer energy within the gap separating the two arms, forming the peak in shuttle arm temperature seen in Figure 6.2.

6.2 Effect of Shuttle Thermal Expansion

The increase in shuttle temperature due to the heat transfer within the gas will inevitably lead to errors in the Knudsen force measurement as a result of thermal expansion. To quantify this effect the temperature distribution along the length of the shuttle is first extracted from the thermal images. The total shuttle expansion due to temperature variations along its length can then be computed using

$$\Delta L_{shtl} = \frac{1}{2} \sum \alpha_i(T)(T_i - T_{ref})L_i \tag{6.1}$$

The factor of 1/2 in equation 6.1 is included since the shuttle will expand symmetrically about its center. Since capacitive measurements are performed at one end of the shuttle only half of the total expansion need be considered. The temperature dependent coefficient of thermal expansion is determined by the correlation of Swenson [39]. Model constants can be found in Table B.3 of Appendix B.

$$\alpha(T) = \alpha_3 + A_3 \frac{\theta_E^2 e^{\frac{\theta_E}{T}}}{(T(e^{\frac{\theta_E}{T}} - 1))^2} + B_3 \frac{(\frac{T}{\phi_0} - 1)^2}{1 + \beta_3 \frac{T}{\phi_0}} \tag{6.2}$$

Using the temperature profiles of the shuttle acquired at each of the sampled pressures the resulting expansion is plotted in Figure 6.3. Using the LIA calibration the expected effect on output voltage is also provided.

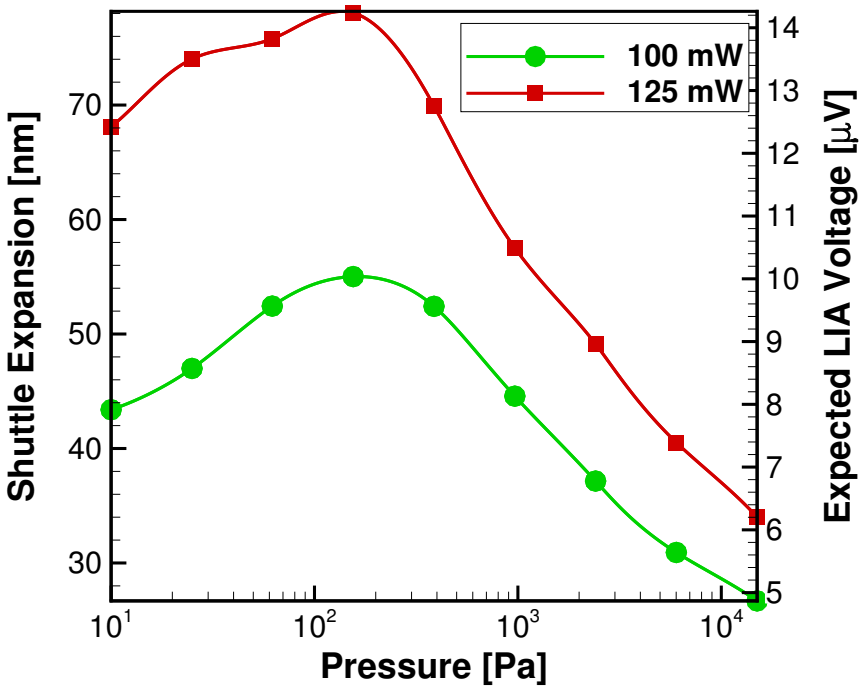

Figure 6.3. Thermal expansion and expected LIA output due to variations in shuttle temperature

As expected from the shuttle arm temperature measurements the thermal expansion peaks near a pressure of 150 Pa, regardless of applied power. By considering the configuration of MIKRA the thermal expansion of the shuttle will tend to cause the separation between sense capacitor combs to increase, an effect which could potentially be misattributed to Knudsen forces. It will be shown in the following chapter that errors introduced to force measurement due to this expansion are small near the

location of peak magnitude but can become appreciable near the upper and lower pressure limits.

6.3 Comparison of Heater Temperature and Resistance Measurements

Platinum was chosen as the heating element material primarily due to its linear variation in resistivity with temperature [21]. By using the thermal microscopy measurements of the MIKRA device during heater engagement the average temperature along the entire length of the heating element can be extracted and compared to the corresponding resistance measurement. Performing this averaging serves as a means of calibration, allowing average heater temperature to be evaluated for an arbitrary resistance. A plot of the resistance measurement as a function of average heating element temperature for heaters A and B at powers of 100 and 125 mW for the measured pressure range is provided in Figure 6.4.

As expected, the heater resistance varies nearly linearly with average temperature, showing a total average sensitivity of 8.24 Ω/C. The results of performing a linear least-squares fit on the data from Figure 6.4 are provided in Table 6.1.

Table 6.1. Linear least-squares fitting parameters and regression coefficients for the heating elements

	Power [mW]	Sensitivity [Ω/C]	R^2
Heater 1	100	8.84	0.984
Heater 1	125	8.53	0.998
Heater 2	100	8.31	0.988
Heater 2	125	7.29	0.992

From these results it can be seen that the average R^2 value for the resistance calibration is 0.991 indicating that the heater resistance varies linearly with the average

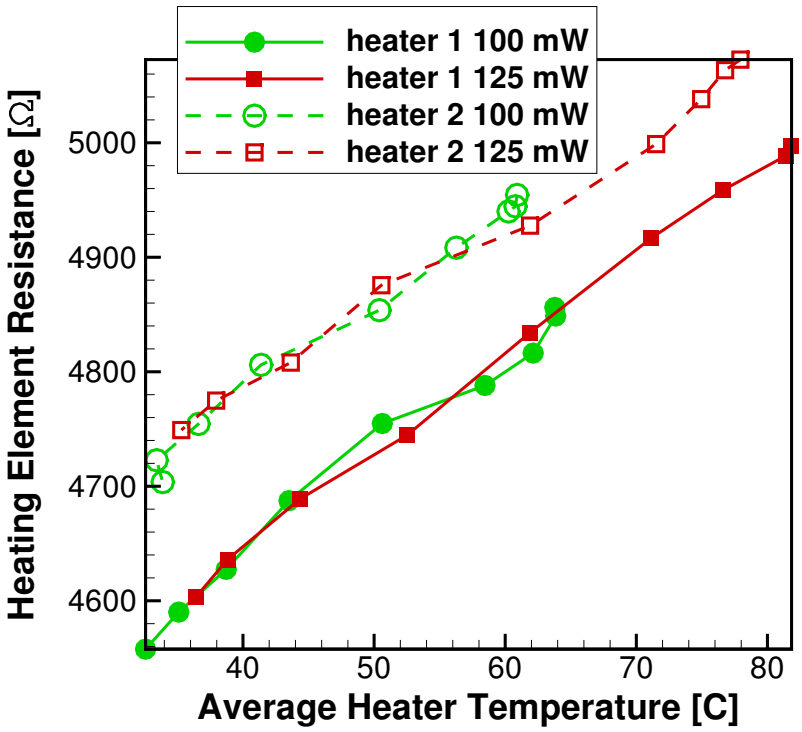

Figure 6.4. Variation in measured heating element resistance with average temperature

temperature, even with the large temperature non-uniformities along the length of the filament.

7. KNUDSEN FORCE QUANTIFICATION

Following the test procedure outlined in Figure 4.4 the shuttle displacements and Knudsen force magnitudes averaged over 5 heating cycles per pressure for both air and helium are shown in Figure 7.1.

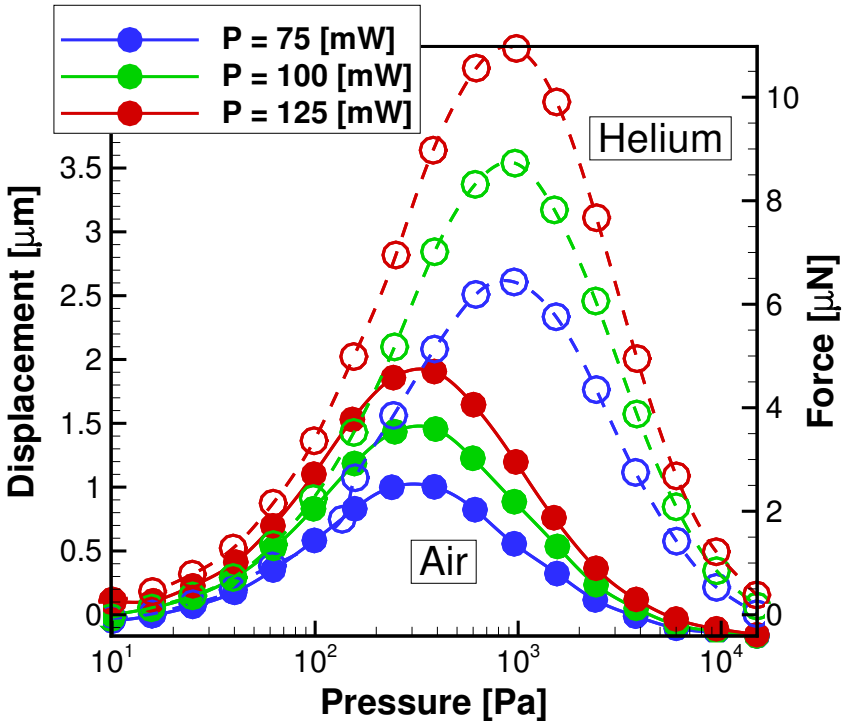

Figure 7.1. Shuttle deflection and Knudsen force magnitude as a function of chamber pressure and heater power for air (solid) and helium (dashed)

The data show an approximate variation of direct and inverse proportion to pressure in the free-molecule and continuum limits respectively. A bell-shaped transition region branches these two regimes. The measurements for air show a peak in LIA output at around 320 Pa regardless of heater temperature, corresponding to a Knudsen

number of around 1.2 with viscosity based on the average temperature of the substrate. Using the LIA calibration the peak signal corresponds to a shuttle deflection of 1.02, 1.48, and 1.92 μm for heater powers of 75, 100, and 125 mW respectively. Peak magnitude increases with increasing heater temperature (power) owing to the greater kinetic energy of the gas molecules within the gap. This variation in peak magnitude with heater power is linear, a behavior which has been observed in a separate study on microcantilevers [20].

Using helium as the working fluid, force peak magnitude moves upward by a factor of around 2.7 with a corresponding outward shift to 875 Pa. Assuming identical chamber thermal conditions as the tests conducted with air the force peak occurs at a Knudsen number of 1.3. The combined magnitude enhancement and peak shift results from the increased mean-free path of helium as well as its higher peculiar velocity, leading to a larger exchange of kinetic energy with the shuttle surface. Similar to the results for air, the variation in peak magnitude is linear with applied power in the peak region and peak signal corresponds to a shuttle deflection of 2.63, 3.54, and 4.45 μm for heater powers of 75, 100, and 125 mW respectively.

The difficulty of extending the measurement range of traditional Knudsen gauges beyond the free-molecule regime lies in the nonlinear variation in force magnitude with increasing ambient pressure. These effects are clearly demonstrated in Figure 7.1 for air at pressures greater than approximately 60 Pa (Kn $\leq$ 8.0) and helium greater than 190 Pa. If used for the purpose of pressure sensing the bell shape of force magnitude results in a measurement which is not unique, thus greatly limiting the operational range. This problem can be overcome however with the aid of the monotonically varying heating element resistance from Figure 6.2.

7.1 Coupling of Heating Element Resistance and Capacitance

As a result of a non-monotonically varying force output with pressure, Knudsen gauges have traditionally been confined to the measurement of pressure for which the

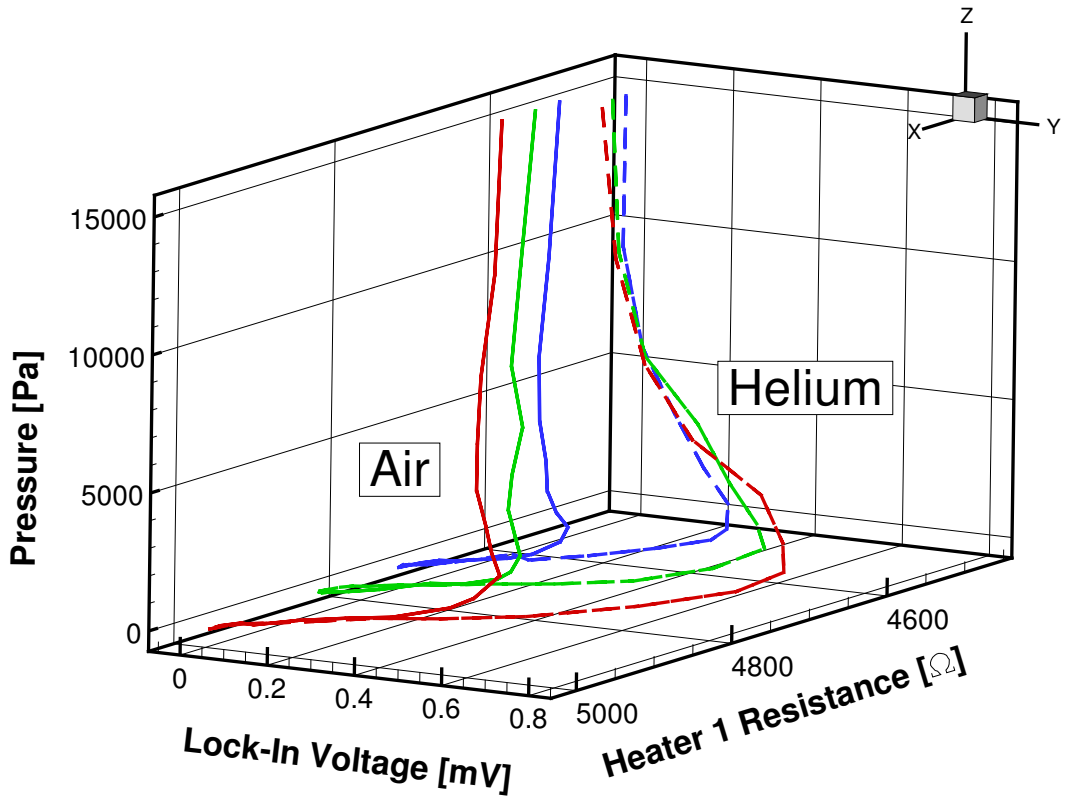

Figure 7.2. Ambient pressure dependence on capacitance and heating element resistance for air and helium

flow is free-molecular. With the introduction of the heating element resistance the force measurement can be uniquely defined at any pressure over which Knudsen forces are significant, extending the measurement range by up to 3 decades. To illustrate this feature, chamber pressure as a function of LIA output and heating element 1 resistance is shown in Figure 7.2.

For low pressures the force output is largely independent of composition, regardless of applied power. This result is consistent with behavior documented in the literature [37, 6]. As pressure is increased the thermal stresses become the dominant force generation mechanism and output becomes highly sensitive to concentration.

If the fluid composition is precisely known (e.g. pure air or helium) the ambient pressure can be determined simply from the resistance and capacitive measurements.

If the gas mixture is binary and of unknown concentration both pressure and composition can still be determined, however this capability necessitates calibration against a series of known concentrations and is out of the scope of this work. This feature is desirable in many practical applications such as the lyophilization of food or pharmaceuticals where water vapor concentration is used to evaluate drying progress [8]. The measurement of gas properties in these systems is typically performed using only a few transducers, often located far from the product. Low-profile gas-property sensors such as MIKRA not only enable the installation of dozens of sensors throughout the process chamber but also consolidate several sensing mechanisms onto a single integrated platform.

7.2 Effect of Shuttle Thermal Expansion on Force Measurement

Comparing the LIA output voltage in Figure 7.1 for air to the expected output error due to thermal expansion in Figure 6.3 it can be seen that the expansion effect is comparable to the LIA signal at the upper and lower bounds of the pressure range but accounts for less than 4% of the total output at the peak force location of around 310 Pa. To prove conclusively that thermal expansion is not the root cause of the observed LIA output the sample was placed under the DCM8 microscope and the device motion was observed under the action of only the heating elements. Pressure was regulated at an arbitrarily selected value of 500 Pa. Images of the combs were captured both before and after heater engagement and their difference measured. The images with power off and on with corresponding measurements are shown in Figures 7.3a and 7.3b respectively.

Averaging over all combs the change in finger engagement between powered and unpowered heater states is 1.49 μm. Comparing this directly measured value to that inferred from the LIA output in Figure 7.1 of 1.34 μm under the same conditions

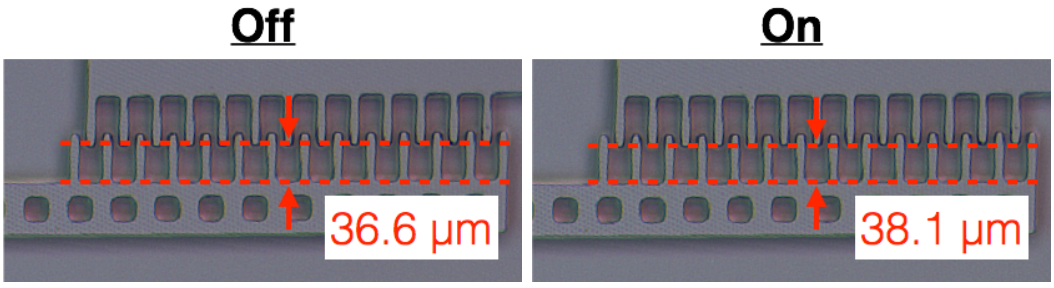

(a) Heating elements off (b) Heating elements on

Figure 7.3. Comparison of comb engagement between heater states for an ambient pressure of 500 Pa

the results agree to within 10%. Considering the location of the actuation combs on the MIKRA device thermal expansion would act to decrease the separation between the shuttle and capacitor arms. This effect is not observed as application of power to the heating elements clearly leads an increase in separation, a result which can be explained only by the influence of Knudsen forces.

7.3 Comparison to Free-Molecular Solution

Using the averaged wet area temperature from Figure 6.2, the experimental results from Figure 7.1 can be directly compared to the free-molecular solution of Knudsen from equation 1.2. These data are provided in Figure 7.4 for ambient pressures less than 300 Pa.

The free-molecular Knudsen gauge solution from equation 1.2 corresponds to the ideal case of complete gas-surface accommodation and therefore serves as the asymptotic limit for the experimental data. For low pressures ($P_\infty \leq 26$ Pa), the slopes of the least-squares fit experimental and theoretical data match quite well, agreeing to within 4.5% and 1% for heater powers of 100 and 125 mW respectively. As expected, for higher pressures ($P_\infty \geq 60$ Pa) the flow becomes influenced by thermal stresses and output behaves non-linearly.

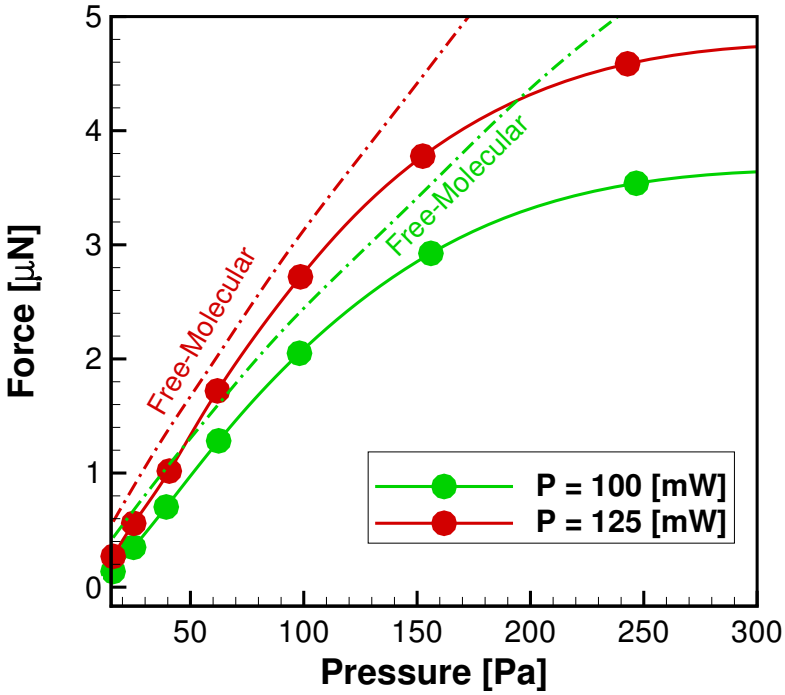

Figure 7.4. Comparison between experimental measurements and free-molecule Knudsen gauge solution

Although Knudsen considered only a pair of isolated plates in his derivation the inclusion of the substrate in the MIKRA device is not expected to contribute to force production provided the temperature of the boundary is the same as that of the far-field, the flow is free-molecular, and the gas interacts diffusely with the silicon. These assumptions are reasonable for the flow conditions surrounding MIKRA and therefore the theoretical solution can be used to approximate force magnitude at low ambient pressures. Nevertheless, higher accuracy approximations accounting for finite body size and incomplete gas-surface accommodation can be obtained following the work of Steckelmacher [37] and Wu [41].

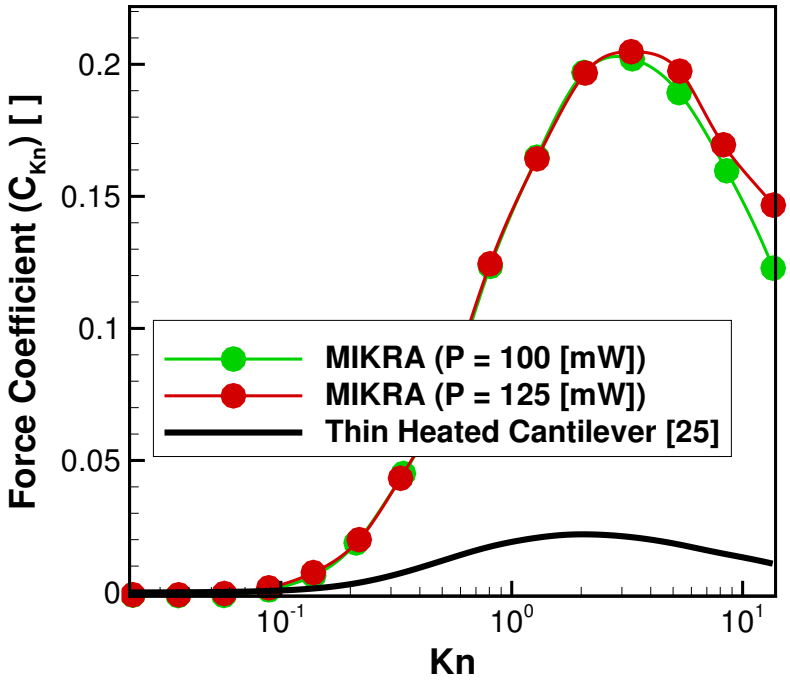

Figure 7.5. Comparison of non-dimensional Knudsen force coefficient for air with numerically derived model [25]

7.4 Knudsen Force Coefficient

Through application of similarity principles the data in Figure 7.1 can be represented in terms of a more general non-dimensional force coefficient [25], C_{Kn}, defined by

$$C_{Kn} = \frac{F_{Kn} T_{shtl}}{P_{\infty}(T_{heat} - T_{shtl}) N_{heat} A} \tag{7.1}$$

The results of the non-dimensionalization for heating element powers of 100 and 125 mW are provided in Figure 7.5. Knudsen number is computed using equation 1.1. The numerical model of Nabeth et al. [25] from equation 2.14 has also been included for comparison.

Clearly, the experimental data demonstrate a consistently higher force coefficient than that predicted using the numerically acquired model for a thin cantilever, showing an enhancement of around 7 times at peak magnitude. The peak location for the experimental data is also seen to be larger, occurring at a Knudsen number of around 3.0. The reason for the larger magnitude and alternate peak location for the experimental data is due to the geometric differences between model and experiment, the former of which consists of a thin cantilever suspended over an infinite substrate. As a result of these discrepancies in thermal gradient configuration this effect is expected to be pronounced at higher pressures where thermal stresses dominate flow behavior. The force coefficients for MIKRA among applied powers agree well between Knudsen numbers of 0.22 and 8.8 with all data falling to within a 6% difference. Outside of this range the small coefficient magnitude leads to larger variations however these limits are very near the generally defined continuum and free-molecule limits, regions where the device is not intended to operate.

8. CONCLUSIONS

In this work I have designed, fabricated, and characterized a Microscale In-plane Knudsen Radiometric Actuator (MIKRA) capable of both producing and quantifying Knudsen forces in a pressure range between 10 Pa and 15 kPa. The design is centered around a movable shuttle mass suspended on a serpentine suspension. Extending transversely from the shuttle are a series of reaction arms running adjacent to a separate set of fixed heating arms. Upon application of electrical power to the heating arms the reaction arms transmit the effect of the thermal stresses developed within the gap, leading to a deflection of the shuttle. This displacement is sensed capacitively by a set of interdigitated combs driven by a charge integrator circuit. A separate set of electrostatic actuation combs provides the capabilities of sensor calibration and dynamic tuning.

Knudsen force magnitude is shown to exhibit strong sensitivity to ambient pressure, behaving non-monotonically between the free-molecule and continuum limits. Peak force output is observed at a Knudsen number of approximately unity when the molecular mean-free path is roughly equal to the gap separating the heating element and shuttle arms. Heating element powers of 75, 100, and 125 mW are tested, the result of which leads to a linear variation of force at peak magnitude. In this case, applied power is directly related to temperature and serves to illustrate MIKRA's sensitivity to thermal gradient within the gap. With the inclusion of the heating element resistance the ambient pressure can be uniquely defined over the entire range of which the Knudsen forces are significant, extending the usable range by 3 decades over existing gauges.

Both air and helium were used as working gases to demonstrate sensitivity to composition. From the results, Knudsen force in the helium environment is enhanced by a factor of 2.4 at peak output, occurring at a pressure 2.7 times greater than that

for air. This behavior stems from the small molecular diameter of helium, leading to an increased mean-free path and peculiar velocity.

Using thermal microscopy, force measurements are presented in terms of a non-dimensional force coefficient, allowing results to be compared directly to existing microscale actuators. The MIKRA device is shown to generate consistently higher force magnitudes than an out-of-plane cantilever configuration, demonstrating an enhancement of around 7 at peak output when the working gas is air. The attributes displayed by MIKRA give this sensing mechanism promise in a variety of sensing applications, namely those involving simultaneous sampling of pressure, temperature, and fluid composition.

8.1 Future Research

At present there exist several planned modifications to improve the performance of the MIKRA device:

- Fabricate separate filaments for each heating arm to facilitate improved thermal management
- Include separate heating elements and temperature sensors to provide more localized temperature regulation
- Increase the box layer thickness to provide additional tolerance to external shock
- Increase initial capacitor engagement as well as the comb finger length to reduce the influence of fringe fields
- Increase the lateral spring stiffness to increase permissible stroke length when using actuation capacitors
- Replace existing sense capacitors with a differential system
- Miniaturize the signal conditioning circuitry to fit onto a single printed circuit board
- Deposit metal material on the shuttle mass to provide more accurate thermal measurements

In terms of fabrication, the improvements listed above will require only marginal modifications to the existing processes. Significant alterations will be required for the signal conditioning electronics, however it is believed these changes will significantly improve the performance of the device, potentially introducing a viable alternative to existing vacuum sensors.

REFERENCES

REFERENCES

[1] G. A. Bird. Molecular gas dynamics and the direct simulation of gas flows. 1994.

[2] J. R. Black. Electromigration: A brief survey and some recent results. *Electron Devices, IEEE Transactions on*, 16(4):338–347, 1969.

[3] S. Chapman and T. G. Cowling. *The mathematical theory of non-uniform gases: an account of the kinetic theory of viscosity, thermal conduction and diffusion in gases*. Cambridge university press, 1970.

[4] W. Crookes. On attraction and repulsion resulting from radiation. *Philosophical transactions of the Royal society of London*, 164:501–527, 1874.

[5] W. Crookes. On repulsion resulting from radiation. parts iii. & iv. *Philosophical Transactions of the Royal Society of London*, pages 325–376, 1876.

[6] J. W. DuMond and W. Pickels Jr. Superiority of a knudsen type vacuum gauge for large metal systems with organic vapor pumps; its design and operation. *Review of Scientific Instruments*, 6(11):362–370, 1935.

[7] G. K. Fedder. *Simulation of microelectromechanical systems*. PhD thesis, University of California at Berkeley, 1994.

[8] F. Franks. Freeze-drying of bioproducts: putting principles into practice. *European Journal of Pharmaceutics and Biopharmaceutics*, 45(3):221–229, 1998.

[9] A. Fresnel. Note sur la repulsion que des corps échauffés execent sur les autres à des distances sensible. In *Annales de Chimie et de Physique*, volume 29, pages 57–62, 1825.

[10] V. Galkin and M. Kogan. Derivation of the equations of slow nonisothermal gas flows. *Fluid Dynamics*, 14(6):873–880, 1979.

[11] M. A. Gallis, J. Torczynski, and D. Rader. A computational investigation of noncontinuum gas-phase heat transfer between a heated microbeam and the adjacent ambient substrate. *Sensors and Actuators A: Physical*, 134(1):57–68, 2007.

[12] N. E. Gimelshein, S. F. Gimelshein, A. D. Ketsdever, and N. P. Selden. Shear force in radiometric flows. Technical report, DTIC Document, 2010.

[13] X. Guo and A. Alexeenko. Compact model of squeeze-film damping based on rarefied flow simulations. *Journal of Micromechanics and Microengineering*, 19(4):045026, 2009.

[14] C. F. Hill. Measurement of mercury vapor pressure by means of the knudsen pressure gauge. *Physical Review*, 20(3):259, 1922.

[15] V. Kaajakari and A. Lal. Thermokinetic actuation for batch assembly of microscale hinged structures. *Microelectromechanical Systems, Journal of*, 12(4):425–432, 2003.

[16] A. Ketsdever, N. Gimelshein, S. Gimelshein, and N. Selden. Radiometric phenomena: From the 19th to the 21st century. *Vacuum*, 86(11):1644–1662, 2012.

[17] M. Knudsen. Thermischer molekulardruck der gase in röhren. *Annalen der Physik*, 338(16):1435–1448, 1910.

[18] M. Kogan, V. Galkin, and O. Fridlender. Stresses produced in gasses by temperature and concentration inhomogeneities. new types of free convection. *Physics-Uspekhi*, 19(5):420–428, 1976.

[19] J. Lee, T. L. Wright, M. R. Abel, E. O. Sunden, A. Marchenkov, S. Graham, and W. P. King. Thermal conduction from microcantilever heaters in partial vacuum. *Journal of Applied Physics*, 101(1):014906, 2007.

[20] A. Lereu, A. Passian, R. Warmack, T. Ferrell, and T. Thundat. Effect of thermal variations on the knudsen forces in the transitional regime. *Applied physics letters*, 84(6):1013–1015, 2004.

[21] D. R. Lide. *CRC handbook of chemistry and physics*. CRC press, 2004.

[22] N. Lobontiu and E. Garcia. *Mechanics of microelectromechanical systems*. Springer Science & Business Media, 2005.

[23] A. E. Lockenvitz. A radiometer-type vacuum gauge. *Review of Scientific Instruments*, 9(12):417–420, 1938.

[24] J. C. Maxwell. On stresses in rarified gases arising from inequalities of temperature. *Philosophical Transactions of the royal society of London*, pages 231–256, 1879.

[25] J. Nabeth, S. Chigullapalli, and A. A. Alexeenko. Quantifying the knudsen force on heated microbeams: A compact model and direct comparison with measurements. *Physical Review E*, 83(6):066306, 2011.

[26] A. Passian, R. Warmack, T. Ferrell, and T. Thundat. Thermal transpiration at the microscale: a crookes cantilever. *Physical review letters*, 90(12):124503, 2003.

[27] A. Passian, A. Wig, F. Meriaudeau, T. Ferrell, and T. Thundat. Knudsen forces on microcantilevers. *Journal of applied physics*, 92(10):6326–6333, 2002.

[28] O. Reynolds. On the forces caused by the communication of heat between a surface and a gas; and on a new photometer. *Philosophical Transactions of the Royal Society of London*, 166:725–735, 1876.

[29] M. Scandurra, F. Iacopetti, and P. Colona. Gas kinetic forces on thin plates in the presence of thermal gradients. *Physical Review E*, 75(2):026308, 2007.

[30] A. Schuster. On the nature of the force producing the motion of a body exposed to rays of heat and light. *Philosophical Transactions of the Royal Society of London*, 166:715–724, 1876.

[31] N. Selden, N. Gimelshein, S. Gimelshein, and A. Ketsdever. Analysis of accommodation coefficients of noble gases on aluminum surface with an experimental/computational method (postprint). Technical report, DTIC Document, 2009.

[32] N. Selden, C. Ngalande, N. Gimelshein, S. Gimelshein, and A. Ketsdever. Origins of radiometric forces on a circular vane with a temperature gradient. *Journal of Fluid Mechanics*, 634:419–431, 2009.

[33] N. Selden, C. Ngalande, S. Gimelshein, E. Muntz, A. Alexeenko, and A. Ketsdever. Area and edge effects in radiometric forces. *Physical Review E*, 79(4):041201, 2009.

[34] S. D. Senturia. *Microsystem design*. Springer Science & Business Media, 2007.

[35] S. V. Sista and E. Bhattacharya. Knudsen force based mems structures. *Journal of Micromechanics and Microengineering*, 24(4):045003, 2014.

[36] Y. Sone. *Molecular gas dynamics: theory, techniques, and applications*. Springer Science & Business Media, 2007.

[37] W. Steckelmacher. Knudsen gauges. *Vacuum*, 1(4):266–282, 1951.

[38] A. D. Strongrich, W. J. O'Neill, A. G. Cofer, and A. A. Alexeenko. Experimental measurements and numerical simulations of the knudsen force on a non-uniformly heated beam. *Vacuum*, 109:405–416, 2014.

[39] C. Swenson. Recommended values for the thermal expansivity of silicon from 0 to 1000 k. *Journal of physical and chemical reference data*, 12(2):179–182, 1983.

[40] D. Wadsworth, E. Muntz, G. Pham-Van-Diep, and P. Keeley. Crookes radiometer and micromechanical actuators. *Rarefied Gas Dynamics*, 1:708–714, 1994.

[41] Y. Wu. Theory of thermal transpiration in a knudsen gas. *The Journal of Chemical Physics*, 48(2):889–894, 1968.

[42] Y. Wu and B. Dutt. Kinetic theory of a modified knudsen's absolute manometer. *Journal of Vacuum Science & Technology*, 9(5):1248–1252, 1972.

APPENDICES

A. Fabrication Recipe

1) LPCVD Nitride Deposition

Equipment: ProTemp Furnace (Tube 2)

Recipe:

- Chamber Pressure: 5 [mT]
- Dichlorosilane: 80 [sccm]
- NH3: 100 [sccm]
- Deposition Time: 76 [min]
- Temperature: 800 [C]
- Thickness (Target): 296 [nm] (250 [nm])

Notes:

- Excellent uniformity, few pinholes present, RI indicates stoichiometric SiN
- Intrinsic stress may prove troublesome for thicker films
- Use 4 buffer wafers upstream of specimen to enhance mixing
- Remove native oxide in BOE immediately before loading
- Etch wafer backside in CF4/O2 plasma (see below)

2) Lithography 1 (Nitride Insulation):

Equipment: Spinner, Suss MA6

HMDS Application:

- Spin Speed: 5000 [RPM]
- Ramp Up: 5 [sec]
- Dwell: 30 [sec]
- Ramp Down: 5 [sec]

PR Application:

- Resist: AZ 9260
- Spin Speed: 5000 [RPM] 6 [um]
- Ramp Up: 5 [sec]
- Dwell: 30 [sec]
- Ramp Down: 5 [sec]
- Soft Bake: 7 [min] @ 100 [C] (hot plate)
- Rehydration: At least 30 min

Alignment and Exposure:

- Exposure TIme: 78 [sec]
- Exposure intensity: 14 [mw/cm^2]

Development:

- Developer: AZ400K:H20 (1:3)
- Develop Time: $\sim$ 80 [sec]
- Hard Bake: 5 [min] @ 145 [C] (HP)

Notes: If mask is contaminated:

- Flood expose backside for 2 min in MA6
- Soak in AZ400K developer (not diluted) for 10 min

3) Nitride Insulation Etch:

Equipment: Panasonic E620

Recipe ($\sim$ 120 nm/min):

- Chamber Pressure: 2 [Pa]
- CF4: 50 [sccm]
- O2: 2 [sccm]
- Etch Time: 1 [min] (6 cycles, 10 sec ea.)
- RF Power: 400 [W]

- Bias Voltage (Platen): 30 [V]

Notes:

- 2:45 + 0:30 - Fully etched

4) Lithography 2 (Heaters):

Equipment: Spinner, Suss MA6

HMDS Application:

- Spin Speed: 3500 [RPM]
- Ramp Up: 5 [sec]
- Dwell: 30 [sec]
- Ramp Down: 5 [sec]

PR Application:

- Resist: AZ 9260
- Spin Speed: 3500 [RPM], $\sim$ 7 [um]
- Ramp Up: 5 [sec]
- Dwell: 30 [sec]
- Ramp Down: 5 [sec]
- Soft Bake: 10 [min] @ 100 [C] (hot plate)
- Rehydration: At least 1 hr

Alignment and Exposure:

- Exposure TIme: 80 [sec]
- Exposure intensity: 14 [mw/cm^2]

Development:

- Developer: AZ400K:H20 (1:3)
- Develop Time: $\sim$ 80 [sec]

Notes:

- Blisters seen, likely due to contamination from nitride deposition/etch
- Thicker resist deposition to enhance liftoff

5) Platinum/Chrome Evaporation:

Equipment: Airco

Recipe:

- Chrome Thickness: 10 [nm]
- Platinum Thickness: 100 [nm]

Notes:

- Preclean using Nanostrip followed by USC Toluene, Acetone, IPA @ 5 min ea.

6) Platinum/Chrome Liftoff:

Equipment: Hot Plate, USC

Primary Lift:

- Solvent: Baker PRS2000
- Temperature: 90 [C]
- Time: Overnight

Secondary Lift:

- Solvent: Acetone
- Time: 30 [sec] in USC

Notes:

- Secondary lift removes fences caused by liftoff
- Do not exceed 30 seconds in USC. Delamination of metallization will occur
- Remove excess PR by placing in Nanostrop (not piranha) for 1 [min]

7) Lithography 3 (Bond Pads):

Equipment: Spinner, Suss MA6

HMDS Application:

- Spin Speed: 3500 [RPM]
- Ramp Up: 5 [sec]
- Dwell: 30 [sec]
- Ramp Down: 5 [sec]

PR Application:

- Resist: AZ 9260
- Spin Speed: 3500 [RPM]
- Ramp Up: 5 [sec]
- Dwell: 30 [sec]
- Ramp Down: 5 [sec]
- Soft Bake: 10 [min] @ 100 [C] (hot plate)

Alignment and Exposure:

- Exposure TIme: 80 [sec]
- Exposure intensity: 14 [mw/cm^2]

Development:

- Developer: AZ400K:H20 (1:3)
- Develop Time: $\sim$ 80 [sec]

8) Gold/Chrome Evaporation:

Equipment: Airco

Recipe:

- Chrome Thickness: 10 [nm]
- Gold Thickness: 50 [nm]

Notes:

- Preclean using Toluene, Acetone, IPA @ 5 min ea. (No USC)
- Liftoff Pt, Cr, Au from exposed areas before STS using Cr etchant
- Immerse for $\sim$ 15 [min]
- Specs noticed on Au bond pads - Result of evaporator itself
- Impact on bondability unknown

9) Silicon Etch

Equipment: STS ASE

Recipe 1 ($\sim$ 2.8 um/min):

- Chamber Pressure: 30 [mT]
  - Etch:
    - SF6: 250 [sccm]
    - O2: 20 [sccm]
    - Cycle Time: 10 [sec]
  - Passivate:
    - C4F8: 30 [sccm]
  - Etch Time: 17 [min] + 1 [min] + 1 [min] + 40 [sec] + 40 [sec] + 40 [sec]
  - RF Power: 1000 [W]
  - Bias Voltage (Platen): 30 [V]

Recipe 2:

- Chamber Pressure: 15 [mT]
  - Etch:
  - SF6: 250 [sccm]
  - O2: 20 [sccm]
  - Cycle Time: 10 [sec]
  - Passivate:

        * C4F8: 30 [sccm]
        * Cycle Time: 10 [sec]
    - Etch Time: 40 [sec] + 40 [sec]
    - RF Power: 1000 [W]
    - Bias Voltage (Platen): 30 [V]

Notes:

- Si from major areas etched after 19 [min] total
- Si remains in small features (release holes and arm gaps)
- Use Recipe 2 after primary etch to permit deeper ion penetration

10) Oxide Etch

Equipment: HF (49%)

Recipe:

- Etch Time: 14 [min]

Notes:

- HF vapor attacks SiN, must perform wet release
- Undercut causes vernier scales to be removed

11) Shuttle Release

Equipment: Critical Point Dryer

Recipe:

- Purge time: 10 [min]

Notes:

- Post release plasma clean in Branson for at least 10 [min]
- Pressure: $\sim$ 900 [mT]
- RF Power: 200 [W]

B. Models Used in Performance Simulations

Knudsen Force Coefficient

Table B.1. Model constants for Knudsen force coefficient [25]

Parameter	**Value**
A_1	38.0535
B_1	5.6832
Γ_1	8.3818
α_1	-0.3835
β_1	-2.3362
γ_1	0.8549

Gas Damping

Table B.2. Model constants for gas damping force [13]

Parameter	**Value**
A_2	10.39
B_2	1.374
α_2	3.100
β_2	1.825
γ_2	0.9660

Thermal Expansivity of Silicon

Table B.3. Model constants for expansivity of silicon [39]

Parameter	**Value**	**Unit**
α_3	-0.687$\times 10^{-6}$	K^{-1}
A_3	5.000$\times 10^{-6}$	K^{-1}
θ_E	685	K
B_3	0.220$\times 10^{-6}$	K^{-1}
β_3	0.316	
ϕ_0	395	K